Current Opinion in Solid State and Materials Science 26 (2022) 100977

Contents lists available at ScienceDirect

Current Opinion in Solid State & Materials Science

journal homepage: www.elsevier.com/locate/cossms

Electrochemo-mechanical effects as a critical design factor for all-solid-state batteries

Yong Bae Song [a], Hiram Kwak [a], Woosuk Cho [b], Kyung Su Kim [b], Yoon Seok Jung [a,*], Kern-Ho Park [b,*]

[a] Department of Chemical and Biomolecular Engineering, Yonsei University, Seoul 03722, South Korea
[b] Advanced Batteries Research Center, Korea Electronics Technology Institute, Seongnam 13509, South Korea

ARTICLE INFO

Keywords:
All-solid-state batteries
Chemo-mechanics
Stack pressure
Solid electrolytes
Mechanical properties

ABSTRACT

All-solid-state batteries (ASSBs) using inorganic solid electrolytes (SEs) are in the spotlight for next-generation energy storage devices because of their potential for outstanding safety and high energy density. Recent progress in this field has been primarily based on advances in materials, such as the discovery of SEs with high ionic conductivities and the improvement of interfacial stability in electrodes. However, the use of inelastic SEs causes severe electrochemo-mechanical failures, such as cathode active material (CAM) disintegration, CAM/SE contact loss, and stress build-up during cycling, deteriorating the Li^+ and e^- transport pathways. Although these concerns have been addressed previously, they have not been contextualized systematically in terms of the mechanical interactions among the components and their impacts on electrochemical performance. Here, we categorize the electrochemo-mechanical effect in ASSBs and its ramifications in terms of stress sources, active materials, composite electrodes, and cell stacks.

1. Overview

The success of the current 4 V lithium-ion battery (LIB) technology is attributed to the development of organic liquid electrolytes (LEs). The use of carbonate-based solvents has enabled the accommodation of state-of-the-art Li salts, such as $LiPF_6$ and lithium bis-trifluoromethanesulfonimide with a high molar concentration of approximately 1.0 M, which meet the requirements of high ionic conductivity and acceptable working temperature [1]. Importantly, organic LEs undergo a self-limiting electrochemical decomposition in the early stage of cell cycling to form unique passivating layers called solid electrolyte interphases (SEIs). This enables the reversible cycling of 4 V-class cathode active materials (CAMs) and a graphite anode with a working potential of approximately 0 V (vs. Li/Li^+); thus a high energy density can be achieved.

Nonetheless, using LEs incurs severe safety concerns, even under controlled operating conditions, as sporadic failure of a single cell could cause the explosion of the battery pack. Thus, much effort has been dedicated to solidifying electrolytes for LIBs [2–10]. In particular, a variety of solid electrolytes (SEs), such as oxides, sulfides, polymers, and their combinations, have been investigated intensively, which has led to noticeable achievements. For example, sulfide SEs with the ionic conductivities exceeding those of LEs have been developed: $Li_7P_3S_{11}$ (1.2×10^{-2} S cm^{-1} at 25 °C) [11], $Li_{10}GeP_2S_{12}$ (1.2×10^{-2} S cm^{-1} at 25 °C) [12], $Li_{9.54}Si_{1.74}P_{1.44}S_{11.7}Cl_{0.8}$ (2.5×10^{-2} S cm^{-1} at 25 °C) [13], and $Li_{5.5}PS_{4.5}Cl_{1.5}$ (9.4×10^{-3} S cm^{-1} at 25 °C) [14–20]. Although these sulfide SEs possess limited electrochemical oxidative stability windows up to approximately 3 V (vs. Li/Li^+)[21–23] this limitation has been addressed by introducing protective coatings on CAM surfaces, such as $LiNbO_3$ [24], Li_2ZrO_3 [8,25], and $Li_{3-x}B_{1-x}C_xO_3$ [26]. Furthermore, recent studies have discovered that halide SEs exhibit exceptionally good electrochemical oxidative stabilities up to 4.3 V (vs. Li/Li^+) with affordable ionic conductivities: Li_3YCl_6 (high crystallinity: 4.0×10^{-5} S cm^{-1}; low crystallinity: 5.1×10^{-4} S cm^{-1} at 25 °C) [27], Li_3InCl_6 (1.49 to 2.04×10^{-3} S cm^{-1} at 25 °C) [28], $Li_2Sc_{2/3}Cl_4$ (1.5×10^{-3} S cm^{-1} at 25 °C) [29], $Li_3Y_{1-x}In_xCl_6$ (1.22×10^{-3} S cm^{-1} at 25 °C) [30], $Li_{3-x}M_{1-x}Zr_xCl_6$ (M = Er and Y, 1.4×10^{-3} S cm^{-1} at 25 °C) [31], $Li_{3-x}Yb_{1-x}M_xCl_6$ (M = Hf and Zr, and 1.5×10^{-3} S cm^{-1} at 25 °C) [32], $Li_{2+x}Zr_{1-x}Fe_xCl_6$ (9.8×10^{-4} S cm^{-1} at 25 °C) [33], and Na_2ZrCl_6 (1.8×10^{-5} S cm^{-1} at 30 °C) [34]. Likewise, hydride SEs, such as $3LiBH_4{\cdot}LiI$ ($\sim 10^{-4}$ S cm^{-1} at 50 °C) [35] and $0.7Li(CB_9H_{10}){\cdot}0.3Li(CB_{11}H_{12})$ (6.7×10^{-3} S cm^{-1} at 25 °C) [36], and garnet-type $Li_7La_3Zr_2O_{12}$ (1.5×10^{-4} S

* Corresponding authors.
E-mail addresses: yoonsjung@yonsei.ac.kr (Y. Seok Jung), kernhopark@keti.re.kr (K.-H. Park).

https://doi.org/10.1016/j.cossms.2021.100977
Received 29 September 2021; Received in revised form 1 December 2021; Accepted 15 December 2021
Available online 30 December 2021

cm^{-1} at 25 °C) [37] with good interfacial stability toward Li metal have also been reported. Overall, in terms of the (electro)chemical properties, the current SE technologies could exceed the requirements of conventional LIB technologies using LEs.

The mechanical properties of SEs are another critical factor in the development of practical all-solid-state batteries (ASSBs) because they affect the effective contact area between SEs and active materials, and in turn, the fabrication methods of electrodes. For example, the application of "brittle" oxide SEs has been highly complicated because they cannot make favorable ionic contacts with CAM without the aid of liquid or polymer electrolytes [6]. In contrast, thick composite electrodes with high mass loadings can be prepared by employing malleable SEs (i.e., sulfides and polymers) and thus deliver high initial areal capacities comparable to those of their LE counterparts [38–40]. However, the inherent characteristics of inorganic solids, that transfer and take up external stresses, have important electrochemo-mechanical effects on the performance of ASSBs [41–46].

Here, the electrochemo-mechanical effects in ASSBs are considered a multiscale subject. The relevant issues are categorized in Fig. 1. Obviously, the practical behavior of ASSBs is more complicated than what we discuss herein because of the irregular distribution of SEs and pores in a cell. The major stress source of ASSBs is the volume change of the active materials upon cycling. Firstly, this creates internal micro-cracks within CAM particles. The accumulation of these micro-cracks eventually results in the "disintegration" of the CAM particles [44,47]. The internal cracks are not taken up by the SEs even under a high external pressure of tens of megapascals (MPa) [44,47]. This is in stark contrast to LIBs, where LEs infiltrate the cracks, and the active contact area is increased upon cycling [44,47–49]. Secondly, the repeated volume expansion/shrinkage of active materials cannot be readily accommodated by the deformation of SEs, which results in the "delamination" of SEs from active materials, thus the effective CAM/SE contact area is decreased [44,47,50]. Furthermore, careful observation at the initial charging stages in a recent study has revealed that a redox reaction of SEs induces localized stresses in composite electrodes [45,46]. These two stress sources, that is, active materials and SEs, collectively give rise to electrochemo-mechanical failures in composite electrodes.

Li plating/stripping on the SE layer, the most prominent stress source, has been extensively studied for ASSB cells utilizing oxides [51–53], sulfides [54,55], and polymers [56–58]. In fact, the Li plating/stripping process is a complex phenomenon in which multiple factors, including morphological aspects (planar vs. dendritic growth) [59], the mechanical robustness of SEs [60,61], and the characteristics of Li^+ flux (magnitude and tortuosity) [62,63] are related. However, the extent of the volume expansion of Li metal and its impact on the stack stress evolution in the cells are the predominant factors for practical cell balancing. For example, the volume expansion ratio upon Li metal plating equivalent to 6 mA h cm^{-2} on a 50-μm-thick Li foil corresponds to + 58%, even for ideal planar Li growth. This is much larger than the volume change ratio for $LiNi_{0.8}Co_{0.1}Mn_{0.1}O_2$ upon charging (−8.1%). Understanding the more complicated micromechanics of Li growth at the Li|SE layer interfaces is vital for the utilization of Li metals, and it has been meticulously reviewed in other papers [64,157–159]. Thus, herein we discuss the Li plating/stripping process only in terms of its impact on macroscopic stack pressure changes in conjunction with the volume change of composite cathodes. This electrochemo-mechanical

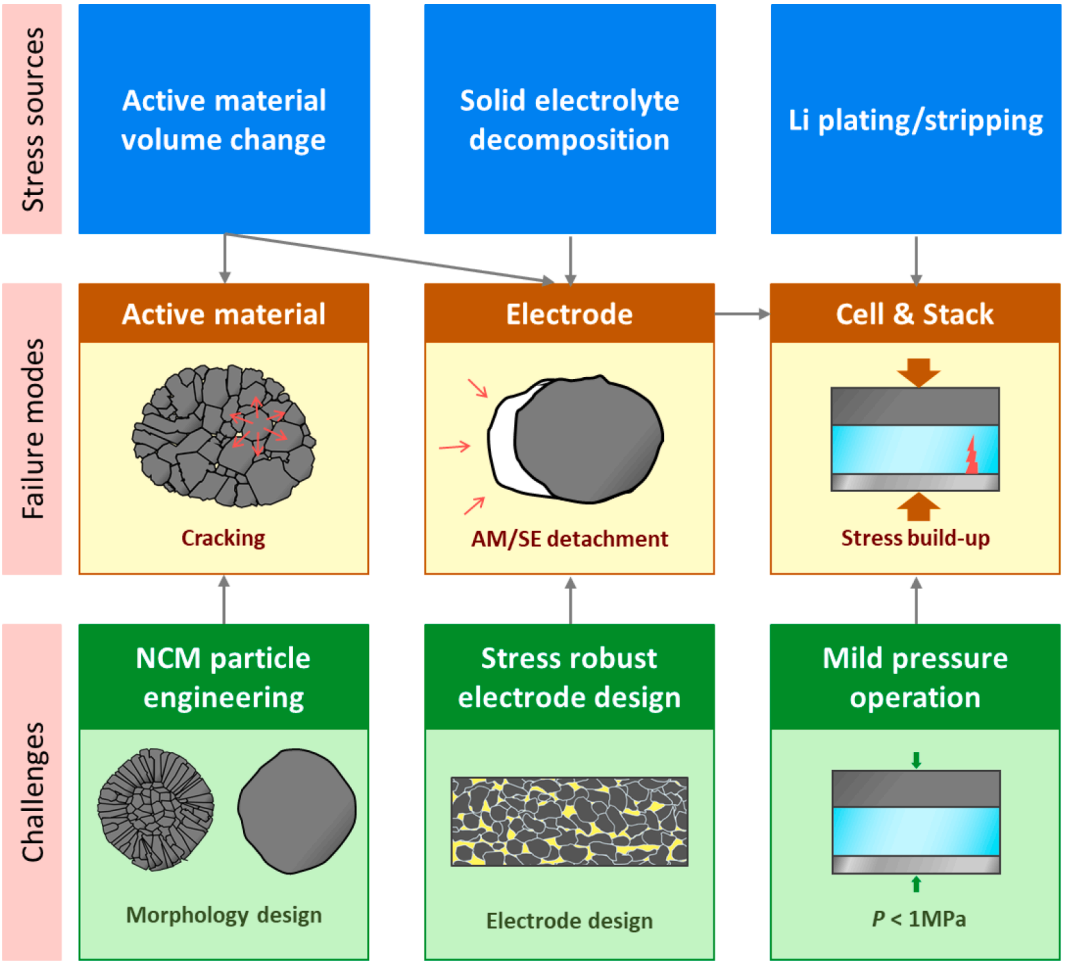

Fig. 1. Categorization of stress sources, possible chemo-mechanical failure modes, and challenges for ASSBs.

cross-talk across the SE layer, the corresponding internal pressure changes, and their counteraction to externally applied pressures are significantly important subjects considering that efficient cell integration is an indispensable advantage of ASSBs.

In the first section, the requirements of SEs for ASSB applications are discussed, highlighting the different mechanical properties of oxide, sulfide, and polymer SEs, and their implications for design factors and fabrication methods for ASSBs. The stress sources causing electrochemo-mechanical effects in ASSBs employing inorganic SEs are summarized in the following section. In addition to the volume changes of active materials upon cycling, which have been extensively studied for LIB applications, the electrochemical SE decompositions are delineated as an important source of local stress. Subsequently, the electrochemo-mechanical failures and corresponding challenges are discussed in terms of active materials, composite electrodes, and full stacks. In the composite electrode scale, the challenges of disintegration of CAM particles and CAM/SE de-lamination upon cycling are described by introducing recent reports. In the last part, the stress cross-talk between the cathode and anode is discussed with the exemplary Li[Ni,Co,Mn]O_2 (NCM)|Li cells according to the extent of external pressurization. The

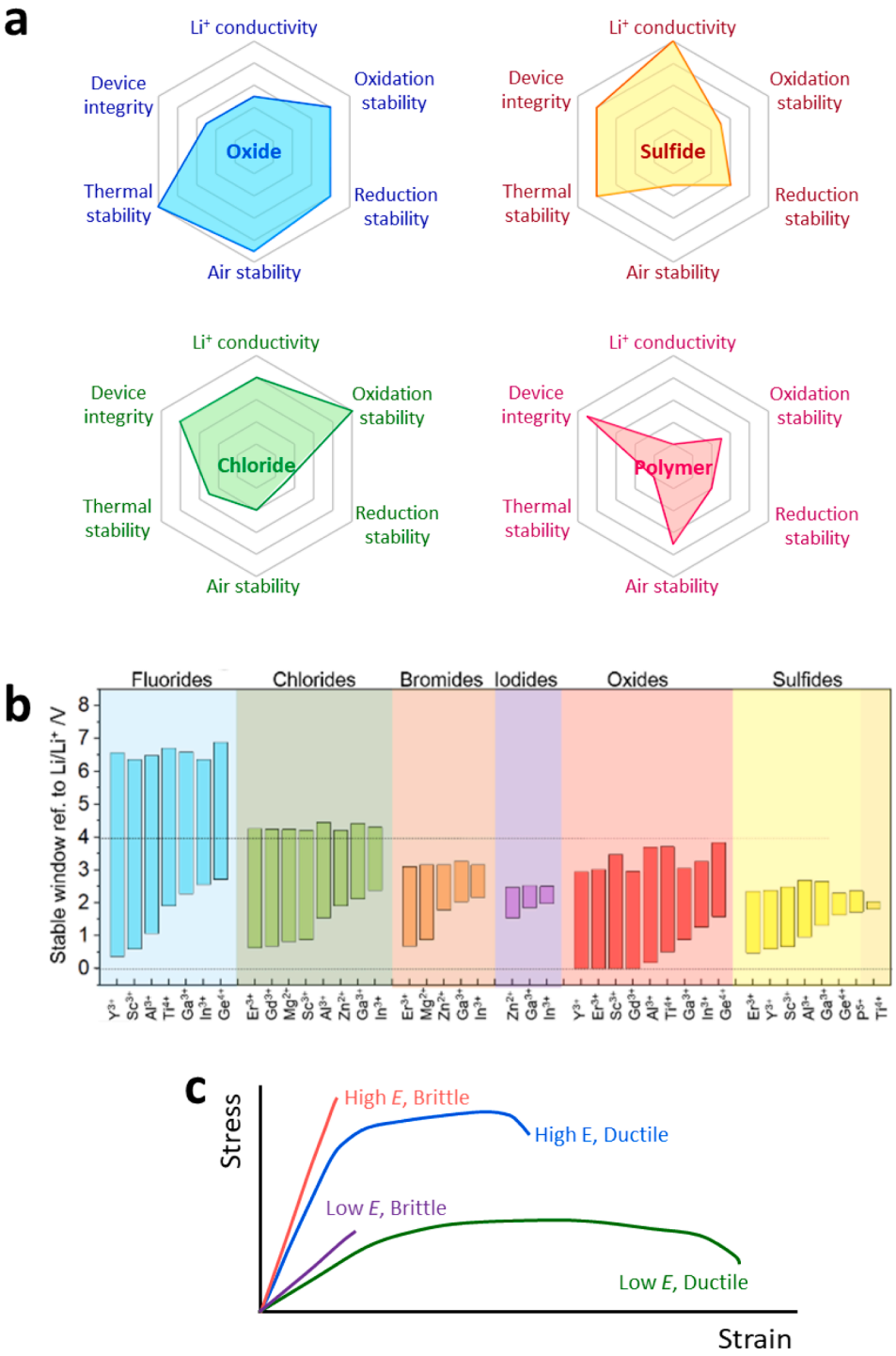

Fig. 2. (a) Comparison of various SE compounds regarding the requirements for ASSB application. (b) Comparison of electrochemical stability windows of inorganic SEs. Reproduced with permission from Ref. [23]. Upper and lower potential limits were estimated by DFT calculations. (c) Typical stress–strain curves for brittle and ductile materials.

mild-pressure operation of ASSBs is a formidable challenge, and many studies have reported promising performance under unrealistically high external pressures (tens of MPa) using a pressure jig [44]. To address this issue, the stack pressure effects on Li plating/stripping are considered. Moreover, to verify the sensitivity of charge carrier conduction in composite electrodes to external pressurization, the tortuosity factors for Li^+ and e^- conduction measured with respect to the various volume ratios of CAM and SE and applied pressures are discussed.

2. Solid electrolytes and cell fabrication methods

2.1. Requirements for solid electrolytes

For advanced ASSB technology, SEs should satisfy multiple requirements, including high ionic conductivity, wide electrochemical stability window, chemical stability toward ambient air, thermal stability, and mechanical properties. Fig. 2a compares the performance characteristics of the four major SEs: oxides, sulfides, chlorides, and polymer electrolytes. Among them, a high ionic conductivity comparable to that of LEs is a prerequisite for room-temperature-operable ASSBs. Oxide SEs exhibit moderate ionic conductivities of approximately 10^{-6}–10^{-3} S cm^{-1} at room temperature [65]. Solid polymer electrolytes (SPEs), where Li salts are dissolved into polymeric matrices, show very low ionic conductivities (~10^{-8}–10^{-7} S cm^{-1} at room temperature) [6]. Incorporating oxide ceramics into SPEs to form composite polymer electrolytes (CPEs) significantly increases the ionic conductivity, which has been attributed to the decreased crystallinity of polymeric domains, interfacial conduction effect, and contribution of oxide SEs [6]. However, their maximum ionic conductivities are two orders of magnitude lower than those of LEs (~10^{-2} S cm^{-1}) [1]. In contrast, a recent search for sulfide and halide SEs has yielded high ionic conductivities, reaching maximums of approximately 10^{-2} and 10^{-3} S cm^{-1}, respectively [4,5,66].

The chemical stability of SEs under humid conditions is important for reliable and cost-effective cell production. Although oxide SEs do not suffer from complete hydrolysis, their surface degradation can severely impede interfacial Li^+ transfer [67]. Sulfide SEs are highly sensitive to humidity and generate toxic H_2S gases [5,68–75]. To alleviate this, the partial substitution of S^{2-} with O^{2-} [76], replacing P^{5+} with Sn^{4+}, which is a softer acid [69,74,77], and adding H_2S scavenging metal oxides [78] have been suggested. Comprehensive reviews on these issues are shown in references [55,79,80].

The viable working voltage of ASSBs is governed by the electrochemical stability of SEs. Poly(ethylene oxide) (PEO)-based SPEs are oxidized starting at 4.0 V (vs. Li/Li^+), which leads to a high interfacial resistance when combined with 4 V-class CAMs, such as $LiCoO_2$ [81]. This interfacial degradation problem is addressed by introducing surface coating layers, such as Li_3PO_4 [81], Al_2O_3 [82], and poly(ethylcyanoacrlate) (PECA) [83]. Mo and co-workers estimated the intrinsic electrochemical stabilities of various inorganic compounds using density functional theory (DFT) calculations [23]. It was predicted that the electrochemical oxidation stability of inorganic materials is determined by the anion species, indicating that the anions are the centers of the oxidative decomposition (Fig. 2b). The order of intrinsic electrochemical oxidation stability in terms of the upper voltage limit is in the order of fluorides > chlorides > bromides ≅ oxides > sulfides ≅ iodides. Sulfide SEs show a very narrow stability limit of approximately 2.5 V (vs. Li/Li^+), which was also confirmed by experimental observations [21,23,84]. The oxidation stability of oxides is largely affected by metal ions. Importantly, chloride SEs were predicted to be stable up to 4.3 V (vs. Li/Li^+), which obviates the protective coatings on 4 V-class layered oxide CAMs. Notably, fluorides exhibit exceptionally high oxidation stabilities (>6 V vs. Li/Li^+), which are offset by their low ionic conductivities. This is owing to the small ionic size and high electronegativity (thus the low polarizability) of F^- [17,23,85]. Importantly, the electrochemical decomposition of SEs has been studied extensively in terms of the formation of resistive decomposition products at interfaces, which explains the practical electrochemical windows [21,23,86]. Their electrochemo-mechanical effect was also highlighted in recent reports [45,46] which will be discussed later.

2.2. Mechanical properties of solid electrolytes

In general, oxide and polymer SEs are considered to be brittle and ductile materials, respectively. Brittle materials tend to have a higher elastic modulus (E) while there are a few exceptions, such as a brittle-to-ductile transition of yttria-stabilized zirconia and a low elastic modulus of ceramic aerosols with yet-brittle properties [87,88]. Also, elastic modulus and ductility are largely affected by grain size, porosity, and dislocation distribution [89,90]. When identical mechanical stresses are applied, brittle materials experience smaller dimensional changes than ductile materials. Beyond the elastic strain limit, brittle materials undergo brief plastic deformation followed by fracturing. In contrast, the dimensions of ductile materials change through plastic deformation. Representative strain–stress curves of different materials are displayed in Fig. 2c. Although the measurement of complete stress–strain curves for inorganic SEs has been scarce, the elastic moduli of various SEs have been experimentally obtained by means of nano-indentation techniques and ultrasonic pulse echo techniques [41,91–93]. There are more quantitative factors that describe the mechanical properties of SE materials. The shear modulus (G) and bulk modulus (K) indicate the resistance of the materials to shear deformation and hydrostatic compression, respectively. Poisson's ratio (ν), which is the ratio of transverse and axial strain, is also an important parameter that describes the compressibility of materials (i.e., $\nu = 0$ for fully compressible materials and $\nu = 0.5$ for incompressible materials).

The mechanical parameters of the major inorganic SEs are listed in Table 1 [91,92,94–97]. Oxide SEs exhibit much higher elastic modulus values [e.g., $LiTi_2(PO_4)_3$: 143.7 GPa, Li_3PO_4: 103.4 GPa, $Li_{1/2}La_{1/2}TiO_3$: 262.5 GPa, $Li_7La_3Zr_2O_{12}$: 149.8–175.1 GPa] [95] than other compounds, which reflects the brittleness of oxides. However, as an exception, several glass oxide SEs can be deformed by cold pressing, forming two-dimensional (2D) contacts with CAMs ($90Li_3BO_3{\cdot}10Li_2SO_4$: 1.0 × 10^{-5} S cm^{-1} [98] and $42Li_2SO_4{\cdot}28Li_2CO_3{\cdot}30LiI$: 5.9 × 10^{-6} S cm^{-1} at 25 °C) [99]. Because of their low elastic modulus values, sulfide SEs are considered to be among the most ductile inorganic SEs (e.g., β-Li_3PS_4: 29.5 GPa [95], $75Li_2S{\cdot}25P_2S_5$: 23 GPa [92], $Li_7P_3S_{11}$: 21.9 GPa [95], and Li_6PS_5Cl: 22.1 GPa [95]). In particular, it is known that sulfide SEs in glass form are more deformable than their crystalline counterparts [92,100–102]. Tatsumisago and co-workers measured the mechanical parameters of thiophosphate glasses by the ultrasonic pulse echo technique and showed that $75Li_2S{\cdot}25P_2S_5$ glass became softer as it accommodated softer ions of I^- and Br^- [92]. This is rationalized by the reduced ion packing density and increased lattice polarizability by incorporating larger anions [69,92,103]. Newly emerging halide SEs are another class of ductile SEs. Recent DFT calculations have shown that the deformability of chloride SEs is not as good as that of sulfides, but bromide SEs show comparable deformability [97].

The fabrication protocol of ASSB cells is highly dependent on the mechanical properties of SEs. Layered NCM or $Li[Ni,Co,Al]O_2$ (NCA) are indispensable CAMs for ASSBs. Because they are brittle oxides, oxide SEs cannot form 2D contacts with them by a simple pressing method [104]. Moreover, the hot-sintering process is problematic because it causes unwanted interfacial side reactions [99]. The most conventional approach to integrating oxide SEs is the fabrication of thin-film ASSBs, which are difficult for mass production targeting large-scale applications such as electric vehicles [105]. Another common practice for tailoring ASSBs using oxide SEs has been hybridization using LEs and/or polymer electrolytes [6,58,106,107]. Recently, several strategies have been suggested to bypass hybridization with organic species. Hu and co-workers suggested a protocol for infiltrating three-dimensional (3D) oxide SE hosts with Li metal [108]. Infiltration methods for cathodes,

Table 1
Mechanical properties [elastic modulus (E), Poisson ratios (ν), shear modulus (G), and bulk modulus (K)] of inorganic SEs.

	Solid electrolytes	Elastic modulus (E, GPa)	Poisson ratio (ν)	Shear modulus (G, GPa)	Bulk modulus (K, GPa)	Method	Ref.
Oxides	$LiTi_2(PO_4)_3$	143.7	0.25	57.6	95.0	Calculation	[95]
	Li_3PO_4	103.4	0.26	40.9	72.5	Calculation	[95]
	$Li_{1/2}La_{1/2}TiO_3$	262.5	0.26	104.0	183.5	Calculation	[95]
	$Li_7La_3Zr_2O_{12}$	175.1	0.27	68.9	127.4	Calculation	[95]
	$Li_7La_3Zr_2O_{12}$	149.8	0.257	59.6	102.8	Indentation	[94]
	Al-$Li_7La_3Zr_2O_{12}$	150.3	–	59.8	–	Indentation	[96]
	Ta-$Li_7La_3Zr_2O_{12}$	153.8	–	61.2	–	Indentation	[96]
Sulfides	β-Li_3PS_4	29.5	0.29	11.4	23.3	Calculation	[95]
	β-Li_3PS_4	–	–	5–6	10–12	Indentation	[91]
	$75Li_2S$-$25P_2S_5$	23	0.32	8.7	21	Ultrasonic pulse echo	[92]
	$80(0.75Li_2S$-$0.25P_2S_5)$-20LiI	20	0.32	7.7	18	Ultrasonic pulse echo	[92]
	$80(0.75Li_2S$-$0.25P_2S_5)$-20LiBr	22	0.33	8.2	22	Ultrasonic pulse echo	[92]
	$80(0.75Li_2S$-$0.25P_2S_5)$-20LiCl	21	0.33	7.8	20	Ultrasonic pulse echo	[92]
	γ-Li_3PS_4	33.4	0.33	12.6	32.9	Calculation	[95]
	$Li_7P_3S_{11}$	21.9	0.35	8.1	23.9	Calculation	[95]
	$Li_{10}GeP_2S_{12}$	21.7	0.37	7.9	27.3	Calculation	[95]
	Li_6PS_5Cl	22.1	0.37	8.1	28.7	Calculation	[95]
	Li_6PS_5Br	25.3	0.35	9.3	29.0	Calculation	[95]
	Li_6PS_5I	30.3	0.33	11.3	29.9	Calculation	[95]
Chlorides	Li_3ScCl_6	46.92	0.265	18.53	33.41	Calculation	[97]
	Li_3YCl_6	38.11	0.274	14.95	28.19	Calculation	[97]
	Li_3ErCl_6	38.64	0.258	15.36	26.63	Calculation	[97]
Bromides	Li_3ScBr_6	27.71	0.240	11.17	11.17	Calculation	[97]
	Li_3YBr_6	23.49	0.194	9.84	9.84	Calculation	[97]
	Li_3ErBr_6	24.08	0.255	9.59	9.59	Calculation	[97]

using $LiCoO_2$ (LCO) gel, LCO precursor solutions, and NCM slurries with or without additives have been suggested [109–111]. Nevertheless, the resulting performances have been highly unsatisfactory owing to the low mass loadings of active materials, low C-rate operation, the high thickness of 3D frameworks, and poor cycling retention when operating at more than 4 V [22,104,112–115]. Moreover, proper CAM candidates are limited, which is related to the high sintering temperatures. Eichel and co-workers reported all-phosphate ASSBs that were fabricated by cold isostatic pressing (CIP), thus minimizing the detrimental interfacial reactions [116]. However, the resulting performance was also far from the practical level. In contrast, the deformable mechanical properties of sulfide SEs ($5 < E < 12$ GPa) allowed them to be easily integrated for the assembly of ASSBs by the cold pressing method, which has also been the case for halide and hydride SEs [36,66].

The mechanical properties also affect the size controllability of ceramics. Ceder and co-workers proposed a quantitative model to determine the effective particle-size ratio of CAM to SE [117]. They suggested that the particle size of SE should be small enough for full capacity utilization. For example, the particle-size ratio of CAM to SE for 98% CAM utilization was estimated to be 2.1 when the weight ratio of CAM to SE was 75:25. Nonetheless, a smaller particle size of CAM is also required to construct the electron pathways and reduce the diffusion length inside the CAM particles [118]. Janek and co-workers reported that $LiNi_{0.6}Co_{0.2}Mn_{0.2}$ particles with a mean particle size (D_{50}) of 4.0 μm outperformed those with larger D_{50} (15.6 and 8.3 μm) [118], which indicates an optimal SE particle size of less than 1.9 μm. It would decrease further as a higher weight ratio of CAM is required for higher energy density. The particle size of "brittle" oxides could be reduced to less than 100 nm by simple mechanical pulverization, such as ball milling and jet milling [119,120]. However, to the best of our knowledge, pulverized sulfide SEs with $D_{50} < 1$ μm have been scarce thus far. This large difference in particle sizes between oxide and sulfide SEs is related to their different responses to the mechanical collisions that occur during the pulverization process and reflects the fact that oxides and sulfides undergo brittle fracture and ductile fracture, respectively. It should be noted that most sulfide SEs with high ionic conductivities (e.g., >1 mS cm^{-1} at 25 °C) can be synthesized at a temperature high enough to cause particle growth (>450 °C). Thus, the development of a scalable particle-size reduction method considering the ductile properties of SEs is imperative.

Recently, Janek and co-workers demonstrated that the ductility of sulfide SEs (β-Li_3PS_4 and Li_6PS_5Cl) are affected by crystallinity, causing different cycling performances [43]. Similarly, $Li_2S{\cdot}P_2S_5{\cdot}LiI$ glasses with improved formability exhibited better cycle retention than $Li_2S{\cdot}P_2S_5$ glasses when used for silicon composite electrodes [92]. The increased brittleness of SEs with increasing crystallinity accounted for each failure mode. Detailed results are introduced in Section 4.2. Monroe and Newman proposed that dendritic Li growth owing to SE|Li interfacial roughening can be suppressed when the shear modulus of the SE layer is higher than 8.5 GPa [60]. Overall, the mechanical properties of inorganic SEs affect the ASSB fabrication method, the particle-size controllability of SEs, and the electrochemo-mechanical behavior of ASSBs during cycling.

3. Sources of electrochemo-mechanical effects

3.1. Volume change of active materials

The volume change and spatial strain distribution of active materials during cycling is a significant issue for conventional LIBs [121,122]. The volume change values during electrochemical cycling for various active materials are summarized in Table 2.

Layered $LiMO_2$ (M = Ni, Co, Mn, Al, etc.) with an α-$NaFeO_2$ structure with a space group $R\bar{3}m$ has been the major CAM for both advanced LIBs and ASSBs [123–125]. Although first-generation $LiCoO_2$ has a theoretical capacity of 270 mA h g^{-1}, the structural irreversibility (hexagonal to monoclinic) and the interfacial instability upon extracting>0.5 mol of Li has limited its practical capacity to approximately 145 mA h g^{-1} [124,125]. Upon charging $Li_{0.5}CoO_2$, the unit cell volume of $LiCoO_2$ increases by +2% [126].

Layered NCM and NCA with higher theoretical capacities than $LiCoO_2$ show distinctive electrochemo-mechanical behavior depends on Ni-contents [127,128]. As the Ni-content increases for NCM, the amount of volume change tends to increase [129]. In fact, $LiNi_{1/3}Co_{1/3}Mn_{1/3}O_2$ show a volume change of only 1–2% [130,131] which is in contrast to a maximum of 10% for Ni-rich NCMs or NCAs [125,127,128,132,133]. It

Table 2
Reaction equations of active materials for lithium batteries and corresponding theoretical capacities and volume changes.

Reaction	Capacity (mAh/g)	Volume change (%)	Ref.
$LiCoO_2 = 0.5Li + Li_{0.5}CoO_2$	135	1.9	[121,122,126]
$LiFePO_4 = Li + FePO_4$	170	−6.5	[121]
$LiFePO_4 = Li + FePO_4$	170	−7.2	[122]
$LiMn_2O_4 = Li + 2MnO_2$	120	−7.3	[121],
$LiMn_2O_4 = 1.85Li + Li_{0.15}Mn_2O_4$	120	−6.8	[122]
$Li[Ni_{1/3}Co_{1/3}Mn_{1/3}]O_2 = xLi + Li_{1-x}[Ni_{1/3}Co_{1/3}Mn_{1/3}]O_2$	145–157	−3.4	[131]
$Li[Ni_{1/3}Co_{1/3}Mn_{1/3}]O_2 = xLi + Li_{1-x}[Ni_{1/3}Co_{1/3}Mn_{1/3}]O_2$	150	−2.8	[132]
$Li[Ni_{0.6}Co_{0.2}Mn_{0.2}]O_2 = xLi + Li_{1-x}[Ni_{0.6}Co_{0.2}Mn_{0.2}]O_2$	170	−5.2	[132]
$Li[Ni_{0.8}Co_{0.1}Mn_{0.1}]O_2 = xLi + Li_{1-x}[Ni_{0.8}Co_{0.1}Mn_{0.1}]O_2$	193	−7.8	[132]
$Li[Ni_{0.8}Co_{0.15}Al_{0.05}]O_2 = xLi + Li_{1-x}[Ni_{0.8}Co_{0.1}Mn_{0.1}]O_2$	200	−5.9	[197]
$Li + C_6 = LiC_6$	372	13.1	[121]
$3Li + Li_4Ti_5O_{12} = Li_7Ti_5O_{12}$	175	0	[121]
$4.4Li + Si = Li_{4.4}Si$	4212	310	[121],
$15Li + 4Si = Li_{15}Si_4$	3590	290	[122]
$4.4Li + Sn = Li_{4.4}Sn$	993	260	[121]
$22Li + 5Sn = Li_{22}Sn_5$	993	273.4	[122]
$xLi + Li\ (50\ \mu m) = Li_{1+x}$	2247*	58.2*	–

* Calculated assuming Li plating equivalent to 6 mAh cm^{-2} on 50-μm-thick Li foil

is also noted that $LiCoO_2$ and Ni-rich NCMs (or NCAs) show the volume change in the opposite direction upon cycling, which is explained by the repulsion forces between the oxygen layers that vary with the transition metal ions [42,134].

Ni-rich NCMs ($LiNi_{1-x-y}Co_xMn_yO_2$, $x + y \leq 0.2$) undergo a series of phase transitions during charging: hexagonal to monoclinic (H1 → M), monoclinic to hexagonal (M → H2), and hexagonal to hexagonal (H2 → H3), which can be identified in differential capacity ($dQ\ dV^{-1}$) profiles and in situ X-ray diffraction (XRD) studies [133,135,136]. In particular, the volume contraction during charge/volume expansion during discharge by the H2 ↔ H3 phase transition near the charge end (~4.2 V) causes severe anisotropic strain and microcracks. Sun and co-workers reported changes in the lattice parameters for Ni-rich NCM from in situ XRD studies. The change in Δa was limited to approximately 2.0%, regardless of the Ni content, whereas Δc increased from − 3.7% to − 7.9% with increasing Ni content during charging [129,133,137]. Regarding microcrack evolution associated with anisotropic strain, the microcracking-induced failure mode for ASSBs is distinctly different from that of LIBs [44]. Owing to the nonflowing nature of SEs, any side reactions at the evolved microcracks are ruled out. However, the effect of microcracking on ASSBs should be more significant in terms of ionic disconnection. Moreover, the anisotropic volume changes in CAMs cause the delamination of SEs. The relevant design strategies for Ni-rich NCM for ASSBs are discussed in Section 4.1.

Graphite, with a theoretical capacity of 372 mA h g^{-1}, has a layered hexagonal arrangement of carbon atoms with a space group of $P6_3/mmc$ (no. 194) [138,139]. In contrast to the quasilinear changes of the unit cell volume for Ni-rich layered oxide CAMs upon charging and discharging, graphite shows nonlinear volume changes, reflecting multistep two-phase reactions through various stages (i.e., 1L, 4L, 3L, 2L, 2, and 1) [42,139–141]. The overall volume expansion of fully lithiated graphite is 13.2% (LiC_6).

$LiFePO_4$ and $Li_4Ti_5O_{12}$ are intercalation-type cathode and anode materials with theoretical capacities of 170 and 175 mA h g^{-1}, respectively, that show flat voltage profiles owing to the two-phase reaction [142–144]. The volume change of $LiFePO_4$ during cycling is approximately 7% [142]. $Li_4Ti_5O_{12}$ is referred to as a zero-strain anode because marginal volume changes occur upon cycling [42,143], which can offer stable cycling performance. Moreover, the zero-strain feature for $Li_4Ti_5O_{12}$ allows them to be used as stable counter electrodes for the pressiometry analysis of working electrodes [42,44–46,145].

Alloying-type materials such as Si and Sn are high-capacity anode materials whose volume change features are decisive for reversibility [146,147]. Si has an extremely high theoretical capacity of 4200 mA h g^{-1}, which corresponds to $Li_{22}Si_5$. However, the fully lithiated phase of Si at room temperature in practice is known as $Li_{15}Si_4$, corresponding to 3579 mA h g^{-1} [146,148–150]. Crystalline Si undergoes amorphization during the first lithiation, and a two-phase reaction to form amorphous Si (Li_xSi) appears near 170 mV vs. Li/Li^+. Further lithiation leads to the crystallization of amorphous Si into $Li_{15}S_4$ below approximately 60 mV vs. Li/Li^+ [147]. The volume expansion of Si in the first lithiation/alloying process is approximately 300% and is anisotropic [146]. Studies on the electrochemo-mechanical behavior of Si for ASSBs are scarce, but several studies have shown its feasibility under high operating pressures [92,145,151–153]. Sn is another attractive alloying-type anode material because of its high theoretical capacity of 993 mA h g^{-1}. Moreover, its volumetric capacity of more than 2000 mA h cm^{-3} is even higher than that of Si and Li metal [147,154]. However, the volume expansion of Sn is also high at approximately 260% [121].

Li metal with a body-centered cubic structure has been regarded as the ultimate anode material owing to its high theoretical capacity of 3860 mA h g^{-1} and the lowest redox potential of −3.04 V vs. standard hydrogen electrode (SHE) [155]. However, its poor reversibility and safety issues stemming from dendritic growth have been formidable obstacles for practical applications [156,157]. The volume change of lithium metal electrodes is governed by the amount of deposited Li. Theoretically, an areal capacity of 5 mA h cm^{-2} corresponds to a Li thickness of 24 μm, assuming conformal and planar deposition. However, the change in the Li thickness in practice is even higher because there are various morphological features, such as whiskers, dendrites, and voids [158,159], which are related to the mechanical properties of the electrolyte, Li diffusivity, defects (e.g., pores, dislocations, grain boundaries, etc.), the electronic conductivity of the SEI layer, and surface impurities [159,160]. This anisotropic Li deposition also affects the electrochemical stability and safety [157]. The detailed mechanism and perspectives of the Li plating/stripping process have been extensively discussed in previous reviews [157–159]. Furthermore, the volume change and morphological features of the Li metal are controlled by external pressure for ASSBs [51,158,160,161] which is not surprising considering the ductility of Li metal. A detailed discussion regarding the effects of stack/operating pressure is introduced in Section 5.

3.2. Solid electrolyte decomposition

Electrochemical degradation of SE and its impacts on the performance of ASSB has been intensively studied in terms of the formation of resistive layers and inter-diffusion of metal ions.[86,104,162] Recently, it has also been revealed that the electrochemical degradation of SEs is also an important source of the electrochemo-mechanical effects [45,46]. Although its impact on the total stack pressure can often be marginal compared to the volume changes of active materials, it should be noted that the resulting stresses arise in a highly localized manner [45,46]. Jung and co-workers carried out *operando* differential electrochemical pressiometry (DEP) studies comparing the electrochemical and mechanical effects of employing $LiI{\cdot}Li_3PS_4$ and $Li_{10}GeP_2S_{12}$ in graphite electrodes [45]. $Li_{10}GeP_2S_{12}$ is unstable at potentials below approximately 0.6 V (vs. Li/Li^+), and its decomposition reaction is easily propagated to bulk SE particle owing to the electronically conductive feature of its reduction products (e.g. Li_3P, Li_xGe) [21,84,86]. This interfacial stress was translated into a significant increase in the internal cell pressure, which is comparable to that originating from Li^+ intercalation into graphite (Fig. 3b). Li and co-workers proposed that the electrochemical stability of SEs is affected by mechanical constriction [163–165]. Computational simulations showed that the electrochemical window of $Li_{10}GeP_2S_{12}$ widened from 1.75 to 2.2 V to approximately

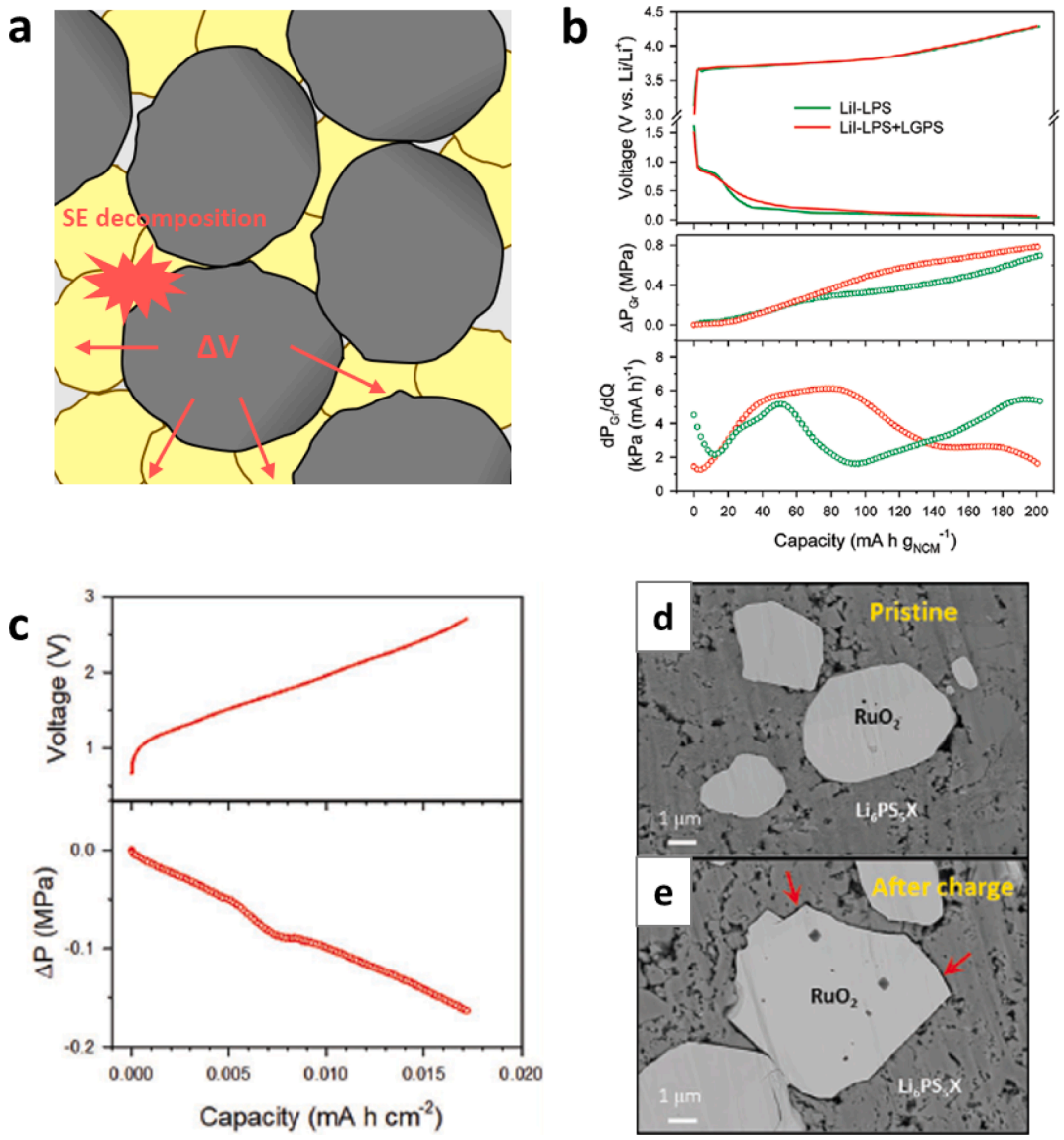

Fig. 3. (a) Stress sources during ASSB cycling. (b) The *operando* DEP results of NCM|graphite cells using only LiI-Li_3PS_4 (LiI-LPS) or both LiI-LPS and $Li_{10}GeP_2S_{12}$ (LGPS) as SEs for graphite electrode. The lithiation voltage profiles, ΔP_{Gr}, and dP_{Gr}/dQ are shown. Reproduced with permission from Ref. [45]. (c) DEP result of RuO_2|LTO cells. Reproduced with permission from Ref. [46]. Cross-sectional SEM image of RuO_2/LPSX composite electrodes (d) before cycling and (e) after charge. Reproduced with permission from Ref. [46].

0.5–2.5 V with increasing pressure from 0 to 20 GPa. They explained these metastable phenomena with the restricted expansion tendency of ceramic sulfides during decomposition under mechanical constraints.

For the cathode, SE oxidation hardly propagates to bulk SE particles, and the corresponding stack pressure change (ΔP) is typically marginal compared with the volume changes of CAMs [46]. Recently, Jung and co-workers designed an *operando* pressiometry experiment using RuO_2/$Li_6PS_5Cl_{0.5}Br_{0.5}$ electrodes [46]. RuO_2 powders with a particle size and electronic conductivity comparable to that of a typical NCM served as a model CAM as these powders do not experience volume change upon charging; only the interfacial side reaction takes place. Fig. 3c shows the charge voltage profile and corresponding stack pressure change of (RuO_2/$Li_6PS_5Cl_{0.5}Br_{0.5}$)|$Li_6PS_5Cl_{0.5}Br_{0.5}$|$Li_{0.5}In$ cells. The small areal capacity was attributed to the oxidation of sulfide SEs on the RuO_2 surfaces. More importantly, a notable decrease in ΔP was detected, implying that the volumetric loss of SE was accompanied by SE oxidation, which was further confirmed by the presence of void spaces at the CAM/SE interface (Fig. 3e). Similar electrochemo-mechanical behaviors have also been detected in NCM|$Li_{0.5}In$ cells by means of *operando* DEP. Janek and co-workers proposed that crystalline SEs are oxidized more significantly than their less-crystalline counterparts because the oxidation reaction is kinetically promoted by the higher electronic conductivities of crystalline SEs [43]. Accordingly, a larger stack pressure drop for crystalline SE oxidation was observed compared with the less-crystalline SE. In practical composite electrodes, even severe SE oxidation takes place on carbon additives [166,167], which also generates local stresses. Although the contribution of SE decomposition to the overall stack pressure is insignificant compared to the volume change of CAM, their dynamic and localized evolution becomes much more significant under a mild external operating pressure, which is discussed in Section 5.2.

4. Challenges for electrodes

4.1. Disintegration of CAMs

Utilizing Ni-rich CAMs for ASSBs is indispensable because they contain lesser amounts of expensive Co and exhibit higher reversible

capacities than $LiCoO_2$. Although $LiCoO_2$ is easily prepared as single-crystalline (monolithic) particles, most commercially available NCM particles show polycrystalline morphology, where randomly oriented primary particles are in tight contact with each other (Fig. 4a) [47,168]. This morphological feature provokes significant electrochemo-mechanical failure of intergranular microcracking [133,169]. This is primarily caused by the anisotropic volume change of the CAM crystallites (i.e., expansion along the *c*-axis and contraction in the *a*–*b*-plane upon delithiation). As the Ni content in NCM or NCA is increased, this anisotropic cell parameter change becomes more significant because Ni ions experience the largest change in ionic size [132]. In addition, the absolute volume change upon charge also increases (e.g., −2.8 % for NCM111, −5.2 % for NCM622, and −7.8 % for NCM811) (Table 2) [132].

For LIBs, LEs infiltrate into NCM particles through intergranular micro- or nano-cracks [48,49]. In addition to this liquid flood, the electrochemical reaction of LEs at disclosed granular surfaces accelerates the disintegration of CAM particles [48,49]. As a result, large cracks are generated across the CAM particles (Fig. 4b) [47,49]. Nonetheless, LEs can wet any exposed granular surface to generate an electrochemically active interface as long as sufficient amounts of LEs are provided. This increases the active surface area for Li^+ transfer, as detected by the increased capacitance in electrochemical impedance spectroscopy (EIS) measurements [48] and by a galvanostatic intermittent titration technique (GITT) study [47]. For an ASSB, SEs cannot flow into the cracks; the cracks remain as void spaces that block intergranular Li^+ diffusion (Fig. 4c) [47]. Eventually, repeated internal cracking leads to the isolation of CAM crystallites (Fig. 4d), which is responsible for the poor initial Coulombic efficiencies and fast capacity fading [44,46].

The quantification of internal cracking was conducted by cross-sectional image analysis [46], the estimation of apparent chemical diffusion coefficients [47,170], and *operando* acoustic emission measurements [171]. Fig. 4d and e display exemplary image analysis

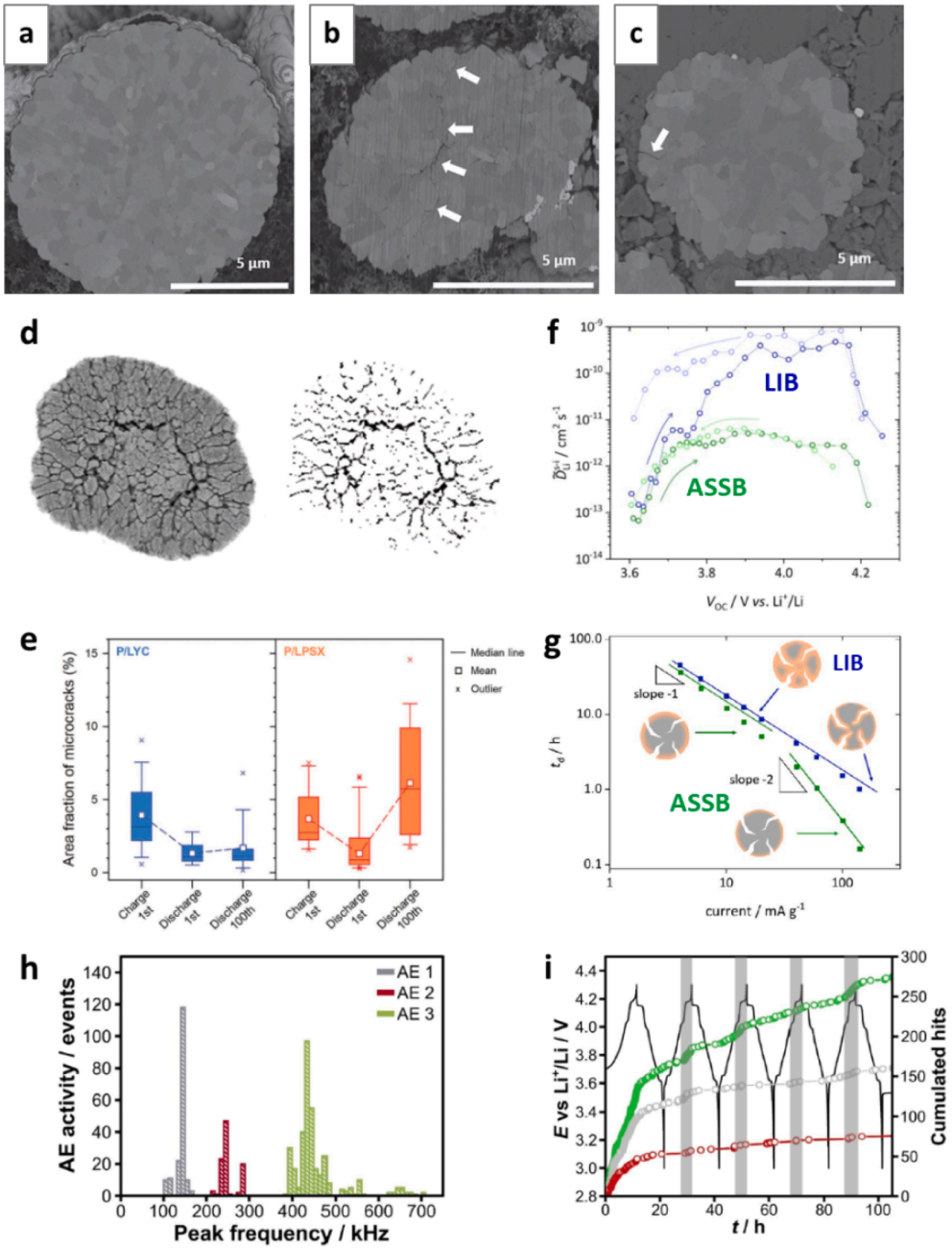

Fig. 4. Cross-sectional images of polycrystalline NCM particles at (a) pristine state, (b) after charging with LE, and (c) after charging with the SE. Reproduced with permission from Ref. [47]. (d) Exemplary image processing for quantification of CAM cracking and (e) its results comparing CAM using the sulfide SE and chloride SE. Reproduced with permission from Ref. [46]. (f) Apparent Li^+ diffusion coefficients measured by GITT in a semi-infinite boundary condition. Reproduced with permission from Ref. [47]. (g) Plot of the discharge time (t_d) and the galvanostatic discharge current comparing LIB and ASSB. Reproduced with permission from Ref. [47]. (h) Accumulated acoustic emission (AE) activity measured during the first five cycle of LIB. Reproduced with permission from Ref. [171]. (i) Cell voltage and corresponding cumulated hits for different frequency bands. Reproduced with permission from Ref. [171].

estimating the areal fraction of internal voids evolved by crack accumulation [46]. In this ex situ analysis, the areal fraction of cracks for charged $Li_{0.88}Co_{0.11}Al_{0.01}O_2$ for electrodes using Li_6PS_5X (LPSX) was estimated to be 3.69%. The crack fraction decreased to 0.90% as the grains expanded at the subsequent full discharge. However, after the 100th cycle, the crack fraction was as high as 6.14%, even in the discharged state, which implied the accumulation of internal cracking upon cycling (Fig. 4e). Janek and co-workers investigated the influence of microcracking on the kinetics of LIBs and ASSBs using an electrochemical method [47]. The apparent chemical diffusion coefficients of cells using sulfide SE and organic LE were measured to be in the same range when both cells were charged up to 3.75 V (vs. Li/Li^+) (Fig. 4f). However, at higher voltages, the cell using organic LE showed a drastic increase in the chemical diffusion coefficient compared to that using sulfide SE. Because the chemical diffusion coefficient is an inherent property of a material, this difference was accounted for by the increased contact area of CAM and LE by internal cracking. It also indicates that the microcracking of the Ni-rich layered oxide was severe when it was charged to more than approximately 4.0 V (vs. Li/Li^+), where the H2–H3 transformation occurs [171,172]. They also measured the relationship between the discharge time (t_d) and discharge current to estimate the kinetic boundary of each system (Fig. 4g). In a double logarithmic plot of t_d vs. current, a slope of −1 was expected for finite diffusion and −2 for semi-infinite diffusion [173]. In contrast to the cell using organic LE, the solid-state cell exhibited semi-infinite diffusion behavior at an increased current range, which implies that full utilization of CAM was not possible in this kinetic environment. In contrast, *operando* detection of CAM cracking is very useful in terms of cell diagnosis under realistic operating conditions and during long-term cycling, which has been very scarce for ASSBs. One applicable technique is acoustic emission measurement, which is often used for LIB diagnosis [171]. For example, Janek and co-workers recently conducted an *operando* acoustic emission study of $LiNiO_2|Li$ liquid cells [171]. Three sound bands (AE1, AE2, and AE3) with different peak frequencies were observed (Fig. 4h). Although AE1 and AE2 were attributed to the formation of a cathode SEI and gas evolution, respectively, AE3 with the

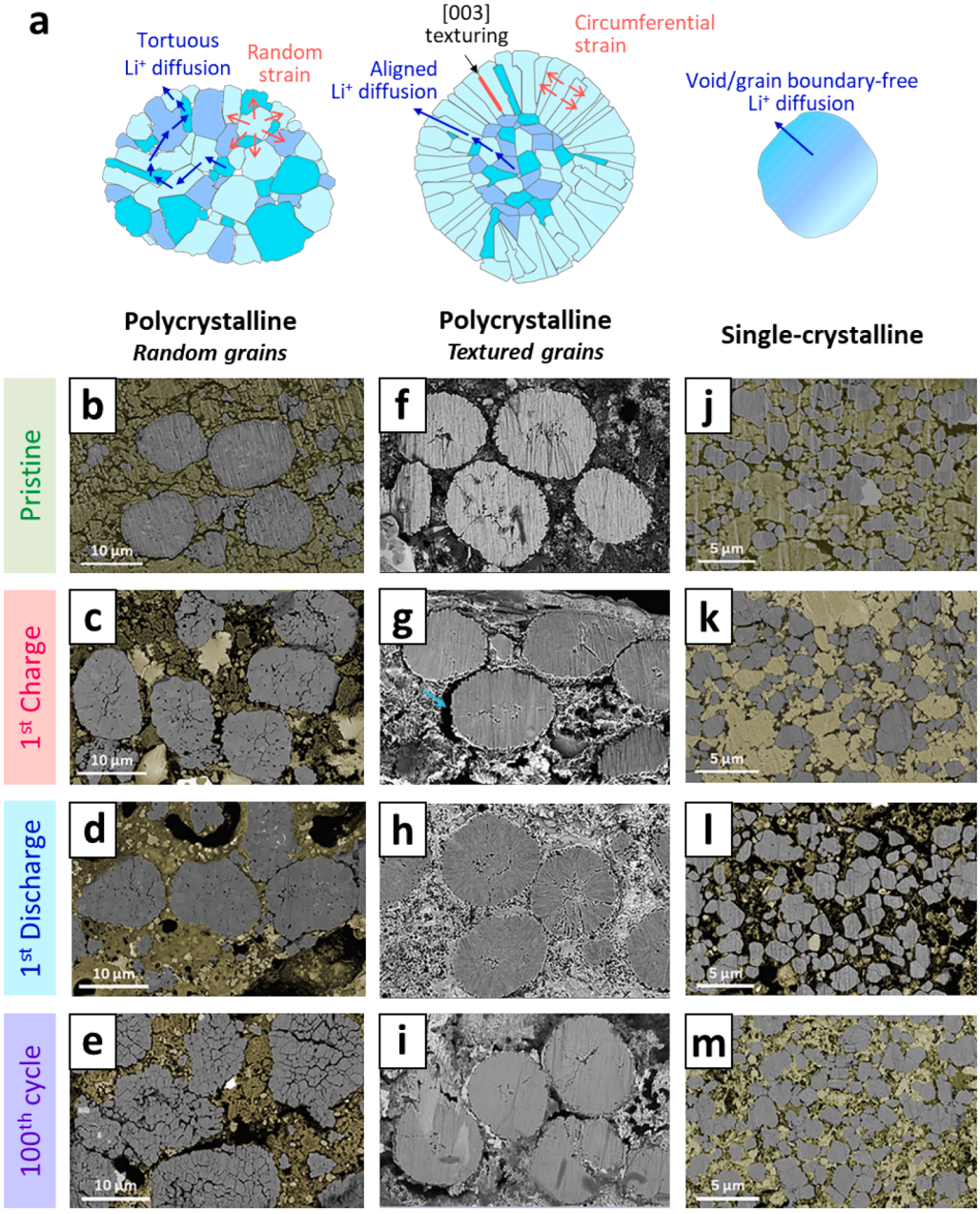

Fig. 5. (a) Schematics of microstructural morphologies showing the generated local stress direction and Li^+ diffusion pathways for polycrystalline CAM particles with randomly oriented grains, textured (radially oriented rod-shaped) grains, and single-crystalline CAM particle. Cross-sectional SEM images of cathodes in ASSBs for (b, f, j) pristine, (c, g, k) after the first charge, (d, h, l) after the first discharge, and (e, i, m) after 100 cycles for polycrystalline CAM particles with (b–d) the randomly oriented grains and (f–h) the textured grains, and (j–l) for single-crystalline CAM particles. Reproduced with permission from Refs. [44,46].

highest peak frequency was assigned to the $LiNiO_2$ cracking as this band accumulated at a high voltage and did not decay upon cycling (Fig. 4i).

For LIBs employing LEs, the electrochemo-mechanical failure of CAMs is mitigated by the use of composition-gradient CAM particles [169,174,175], refining particle sizes [176,177], and designing mechanically compliant morphologies [168,178–180]. Notably, the latter includes CAMs with single-crystalline (monolithic) particles [179] and radially oriented grains [168]. Dahn and co-workers demonstrated that single-crystalline NCM|graphite cells could deliver an excellent cycle life (approximately 4% capacity loss after 4000 cycles) [179]. This exceptional cyclability was attributed to the mechanical robustness of single-crystalline NCM, which led to less microcracking and thereby reduced LE decomposition at the newly exposed internal interfaces [179]. Sun and co-workers synthesized NCM with radially oriented primary particles in which the (0 0 3) plane was energetically stabilized and thus circumferentially aligned [168]. This crystallographic texturing converted a random strain distribution into a uniform circumferential strain distribution that effectively suppressed the local stress concentration and thus the microcracking during cycling [169,174]. These morphological solutions for electrochemo-mechanical failure were also effective for ASSBs [44,181]. Fig. 5a illustrates three CAM particle morphologies: polycrystalline with i) randomly oriented primary particles, ii) radially oriented rod-shaped primary particles, and iii) void-free monolithic particles (single-crystalline). Polycrystalline CAMs with randomly oriented grains showed severe intergranular microcracking, even after the initial charging (Fig. 5c) [44]. The volume fraction of internal cracks decreased after subsequent discharging, but the intergranular contacts were not fully recovered (Fig. 5d). After 100 cycles, the original CAM particle structure was destroyed, and microcracking of the primary particle was also observed (Fig. 5e), which was responsible for the severe capacity loss upon cycling (Fig. 6a) [44]. In contrast, the crystallographically textured CAMs showed marginal internal cracking (Fig. 5f–i). The single-crystalline CAMs were also mechanically robust against the build-up of internal stresses upon cycling (Fig. 5j–m) [44,46].

In addition to the mechanical properties of CAMs, other factors can affect the extent of CAM disintegration. At a given externally applied stack pressure at which internally arising stresses are accumulated, the degree of stress relaxation and resulting stress distribution largely affects the CAM cracking behavior. Jung and co-workers showed that the cycling performance of ASSBs was critically affected by the volumetric fraction of SEs, even when electrochemically stable Li_3YCl_6 and mechanically compliant single-crystalline CAM were used [46]. After 200 cycles, a composite electrode with 29.1 wt% SE (Fig. 6b) showed much more internal microcracks than that with 40.7 wt% SE (Fig. 6c). This severe CAM cracking for the lower SE fraction was rationalized by the increased CAM/CAM (brittle/brittle) contact points at which the stress build-up would be much more significant, compare to CAM/SE (brittle/ductile) contact areas [46]. Accordingly, the composite electrode with 40.7 wt% SE exhibited much better capacity retention than that with 29.1 wt% SE (Fig. 6d).

The Li^+ diffusion behavior in CAM particles is also affected by their morphological features, especially for ASSB applications. For LIBs using LEs, LEs could infiltrate through cracks and wet internal grains, causing Li^+ to diffuse out. In contrast, for ASSBs, Li^+ diffuses only through selected grain boundaries connecting the active planes for Li^+ transfer [cf. (0 0 3) plane]. Consequently, the Li^+ diffusion pathway in polycrystalline CAMs with random orientation is highly tortuous, impeding

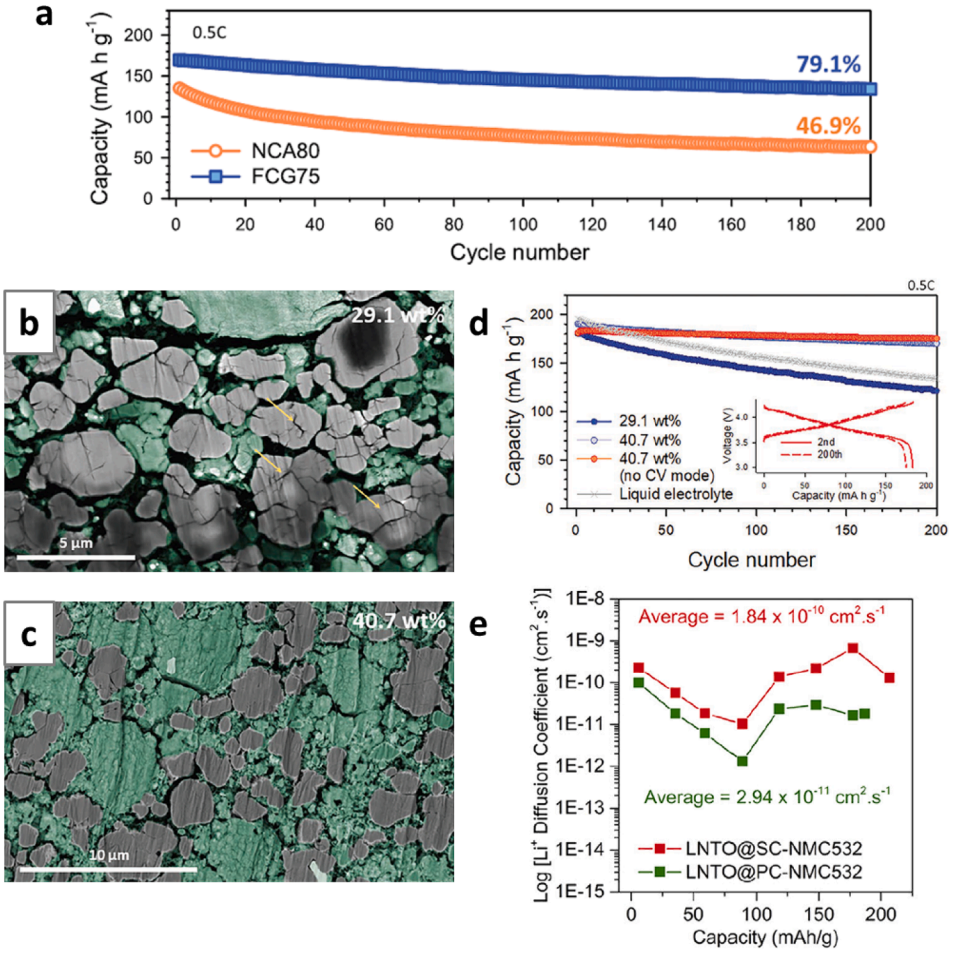

Fig. 6. (a) Cycling performances of ASSBs using polycrystalline CAM particles with randomly oriented and the textured grains. Reproduced with permission from Ref. [44]. Cross-sectional SEM images of composite electrodes using Li_3YCl_6 as an SE with weight fractions of (b) 29.1% and (c) 40.7% and (d) their corresponding cycling performance compared with that for LE cells. Reproduced with permission from Ref. [46]. (e) Comparison of apparent Li^+ diffusion coefficients of composite electrodes using single-crystalline and polycrystalline CAMs. Reproduced with permission from Ref. [170].

fast Li^+ (de-)intercalation (Fig. 5a). The crystallographically textured CAMs possessed highly aligned Li^+ diffusion pathways (Fig. 5a). The void-free feature of the single-crystalline CAM is also beneficial for minimizing the tortuosity for internal Li^+ diffusion (Fig. 5a), as demonstrated by the improved apparent Li^+ chemical diffusion coefficients for the single-crystalline CAM compared to those of the polycrystalline CAM (Fig. 6e) [170].

4.2. Delamination of active materials/solid electrolytes

LE flow can keep up with the volume change of the CAMs, thus maintaining the CAM/electrolyte contact. In contrast, CAM/SE contacts are severely damaged upon cycling because of the inelastic features of SEs. In particular, there is substantial CAM/SE detachment during charge, during which the lattice volume of CAMs contracts. Fig. 7a and b show the cross-sectional scanning electron microscopy (SEM) images of the NCM composite electrodes before and after initial charging (delithiation) [44]. In addition to the internal cracking of CAM, severe delamination of CAM and SE is observed. This disconnection reduces the ionic contact area and eventually results in ionically isolated CAM particles, which significantly exacerbates the rate capabilities and cycle retention of ASSBs.

The extent of CAM/SE detachment upon cycling is affected by not only the volume fraction of SE and the particle morphology of CAM but also by the mechanical properties of the SE [43]. Janek and co-workers suggested that less-crystalline SEs outperformed their crystalline counterparts because the better plasticity could mitigate the CAM/SE contact loss [43]. For example, a composite electrode using glass–ceramic Li_6PS_5Cl showed better cycle retention than that using crystalline Li_6PS_5Cl, despite the inferior ionic conductivity (glass–ceramic Li_6PS_5Cl: 1.01×10^{-3} S cm^{-1}, and crystalline Li_6PS_5Cl: 1.86×10^{-3} S cm^{-1} at 25 °C, Fig. 7c). The EIS analysis for both electrodes showed that the interfacial resistances, which are a function of the contact area and thickness of the cathode electrolyte interface (CEI), remained similar (Fig. 7d). In contrast, the Warburg coefficient (D_w), which is inversely proportional to the contact area, exhibited a much more drastic increase for the electrodes using crystalline Li_6PS_5Cl (Fig. 7e). This result indicates that the composite electrode underwent more severe CAM/SE contact loss when crystalline Li_6PS_5Cl was used.

In addition to the volume shrinkage of CAMs, the oxidative decomposition of sulfide SEs accelerates the CAM/SE delamination [46]. As shown in Fig. 3e, sulfide SE oxidation and the corresponding volume contraction generate void spaces between CAM and SE [46]. This overlooked source for parasitic CAM/SE detachment could be eliminated by using chloride SEs that are known to be electrochemically stable up to 4.3 V (vs. Li/Li^+) [23,33,46]. Fig. 8a shows the initial charge voltage profiles of the composite electrodes using $Li_6PS_5Cl_{0.5}Br_{0.5}$ and Li_3YCl_6 and the corresponding DEP results. The composite electrode using $Li_6PS_5Cl_{0.5}Br_{0.5}$ experienced notable pressure release at the initial charging, which was further clarified in the DEP (dP/dQ) plot (Fig. 8a). This sudden stack pressure drop is attributed to the oxidative decomposition of $Li_6PS_5Cl_{0.5}Br_{0.5}$. In stark contrast, the electrode using Li_3YCl_6 did not show an initial pressure drop, indicating the absence of an electrochemo-mechanical effect originating from the SE oxidation.

In summary, the volume change of CAMs upon cycling induces electrochemo-mechanical failures, internal cracking of CAM particles, and CAM/SE delamination. In addition, SE oxidation at the CAM/SE interfaces generates voids and localized stress changes, which accelerate CAM/SE delamination (Fig. 8b). Thus, there is a need for rational electrode design to alleviate those mechanical failures. Recently, Jung and co-workers systematically compared composite electrodes comprise of single-crystalline/polycrystalline CAM and sulfide/chloride SE.[46] As shown in Fig. 8c, the best capacity retention was achieved when single-crystalline CAM and chloride SE were used. However, it was noted that a higher SE weight fraction was required for the chloride SE (Li_3YCl_6: 2.43 g cm^{-3}) owing to its relatively larger gravimetric density compare to the sulfide SE ($Li_6PS_5Cl_{0.5}Br_{0.5}$: 1.96 g cm^{-3}) [46]. Hence, the discovery of chloride SEs using lighter elements and better distribution of chloride SEs via downsizing and/or coating on CAMs will significantly promote their practical use in ASSBs. A detailed performance comparison of the combinations is shown in Fig. 8d [46].

5. Challenges for cell stack

5.1. Electrodes and stack volume change

According to an externally applied pressure (P_o), the stack pressure ($P_{stack} = P_o + \Delta P_{stack}$), and cell components respond differently to internally evolved pressure. Fig. 9a shows a schematic illustrating the changes in cell dimensions at different applied pressures for NCM/Li cells in which the volume change of Li metal overwhelms that of the NCM electrode. For simplicity, many factors, such as void generation (e.g., CAM and SE cracking) and pore filling (e.g., Li deposition in porous SE layer), were neglected. When the applied pressure is too high, the volume expansion of the cathodes and Li metal is suppressed, and the cell volume tends to be constrained. In this case, the state-of-charge (SOC) change of the cell mostly turns into internal stress build-up that accelerates the cracking of CAM particles and the SE layer. In particular,

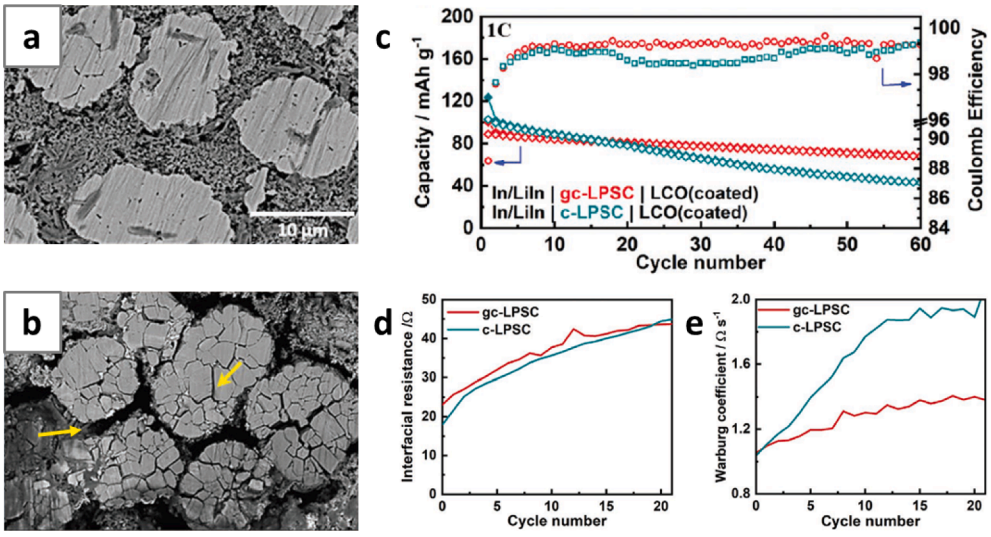

Fig. 7. Cross-sectional SEM images of NCA electrodes in ASSBs (a) before cycling and (b) after the first charge. In (b), the internal cracking and NCA/SE detachment are shown with yellow arrows. Reproduced with permission from Ref. [44]. (c) Cycling performance of LCO/Li-In cells using glass-ceramic-Li_6PS_5Cl and crystalline Li_6PS_5Cl. Reproduced with permission from Ref. [43]. (d) Interfacial resistances between $LiCoO_2$ and solid electrolyte and (e) Warburg coefficients of ASSBs. Crystalline Li_6PS_5Cl or glass–ceramic Li_6PS_5Cl was used as the cathode. Reproduced with permission from Ref. [43]. (For interpretation of the references to colour in this figure legend, the reader is referred to the web version of this article.)

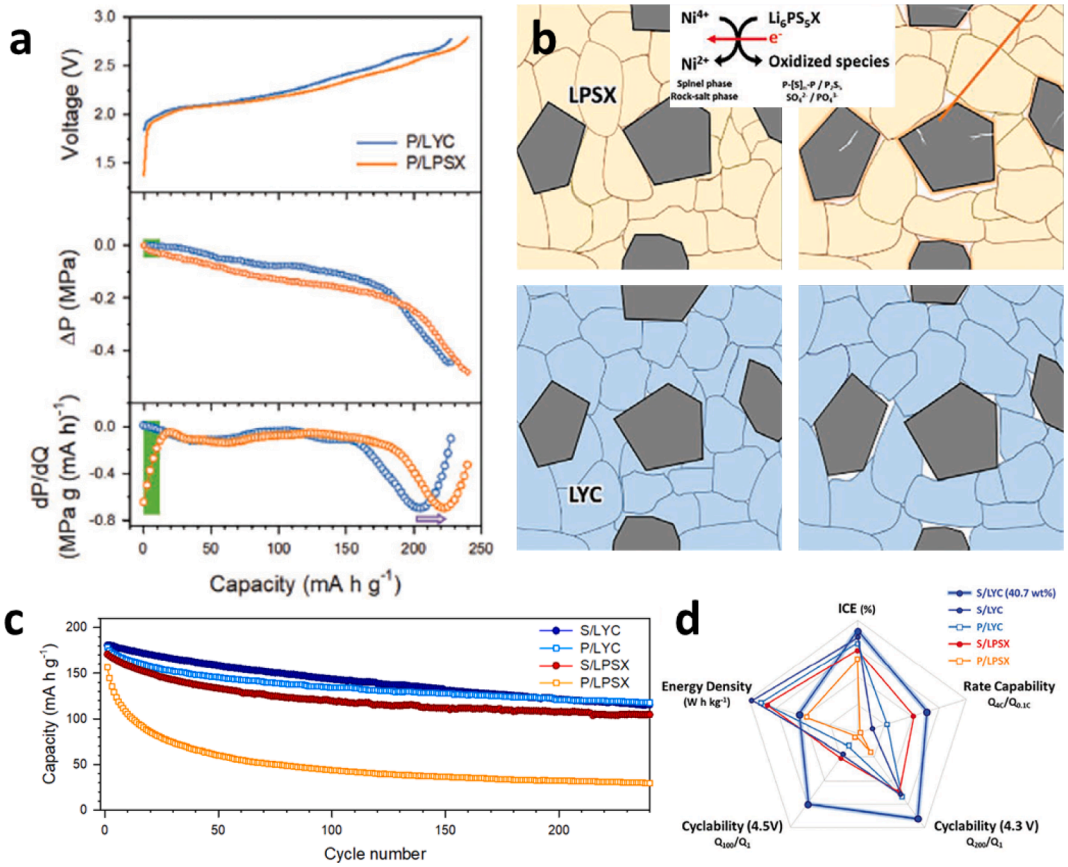

Fig. 8. (a) Initial charge voltage profile, corresponding pressure change, and DEP profiles for polycrystalline NCA electrodes using Li_3YCl_6 (LYC) or Li_6PS_5X (LPSX). Reproduced with permission from Ref. [46]. (b) Schematic illustrating the different microstructural and interfacial evolutions for cathodes in ASSBs, varied with the type of SE (LYC and LPSX). Reproduced with permission from Ref. [46]. (c) Comparison of cycling retention of ASSBs using different CAMs (poly- or single-crystalline) and SE (LYC or LPSX). Reproduced with permission from Ref. [46]. (d) Comparison of the cell performance using different CAMs (poly- and single-crystalline) and SEs (LYC and LPSX). Reproduced with permission from Ref. [46].

the Li deposition process generates localized stresses that induce the cracking of dense SE pellets, although Li metal is far softer (E = 7.82 GPa) than sulfide SEs (E = 23.3–29.0 GPa) [61,95,182]. Because the stresses generated in electrodes cannot be relieved by cell dimensional changes in a volume-constrained cell, the cells fracture easily at high external pressures. Villevielle and co-workers carried out *operando* X-ray tomographic microscopy for a Sn electrode at a pressure of 70 MPa [183]. Under uniaxial compression, cracks initiated from the Sn particles and propagated horizontally, blocking vertical Li^+ migration in the composite electrode [183]. McDowell and co-workers measured the X-ray tomography of $Li|Li_{1+x}Al_xGe_{2-x}(PO_4)_3|Li$ cells, which revealed that the cracks were initiated at the edges of the Li|SE contact area and propagated to the center, followed by the formation of circumferential cracks [184].

When no external pressure is applied, the cathode and Li metal are allowed to readily expand, and the total stack volume is free to increase upon charging (Fig. 9). Thus, only negligible internal stress will be built up. However, under this low operating pressure, CAM/CAM (for e^- transport) and CAM/SE (for Li^+ transport) interparticle contacts in the cathode are easily loosened, which increases the electrode resistance. Moreover, the Li|SE interfacial area is significantly decreased because the rate of plastic deformation of Li metal decreases [51,161,185]. Bruce and co-workers observed Li plating/stripping behavior under low external pressure (3 MPa) using a Li/Li/Li three-electrode cell [161]. Under this mild pressure, the overpotential for Li stripping (current: 1 mA cm^{-2}) gradually increased upon repeated cycling, especially at the end of the stripping, whereas the overpotential for the Li plating processes did not change (Fig. 10a). After a few more cycles, the cell underwent an internal short circuit. When a higher external pressure of 7 MPa was applied, reversible Li plating/stripping was possible up to 100 cycles (Fig. 10b), whereas a short-circuit was observed at a current density of 2 mA cm^{-2} (Fig. 10c). This observation implies that the Li stripping behavior determines the critical current density for dendritic Li growth, and it is critically affected by the applied pressure. Fig. 10d illustrates the suggested failure mechanism of the Li metal anode under a low applied pressure [[161,186]. Because Li metal cannot be deformed under these conditions, the void resulting from Li stripping is not replenished, and the contact area of the Li|SE layer decreases. In subsequent plating, Li deposition is initiated at the triple point of the Li metal, SE layer, and void. Although the void is laterally filled by deposited Li and occluded, dendritic Li growth is expected owing to the concentrated Li flux to the remaining Li|SE interfaces. However, when excessively high external pressure was applied (e.g., >25 MPa), SE layer cracking was induced by Li metal deposition, and internal short circuiting occurred either after applying the initial stack pressure (P_{stack} = 75 MPa) or within a relatively short cycling (P_{stack} = 25 MPa) [187]. Recently, McDowell and co-workers conducted the comprehensive study on the Li|SE|Li cell based on a real-time stack pressure measurement, demonstrating the extent of initial stack pressure critically affects morphological and electrochemical behaviors of Li|SE interfaces [188]. Likewise, the reversibility and rate capability of a Sn electrode are affected by the applied pressure, in which the transformation between Li_7Sn_3 and LiSn is particularly sensitive to pressure [189]. Therefore, it is crucial to search for an optimized stack pressure range for the stable cycling of ASSBs exploiting the Li plating/stripping process.

The volume change of active materials and the corresponding local

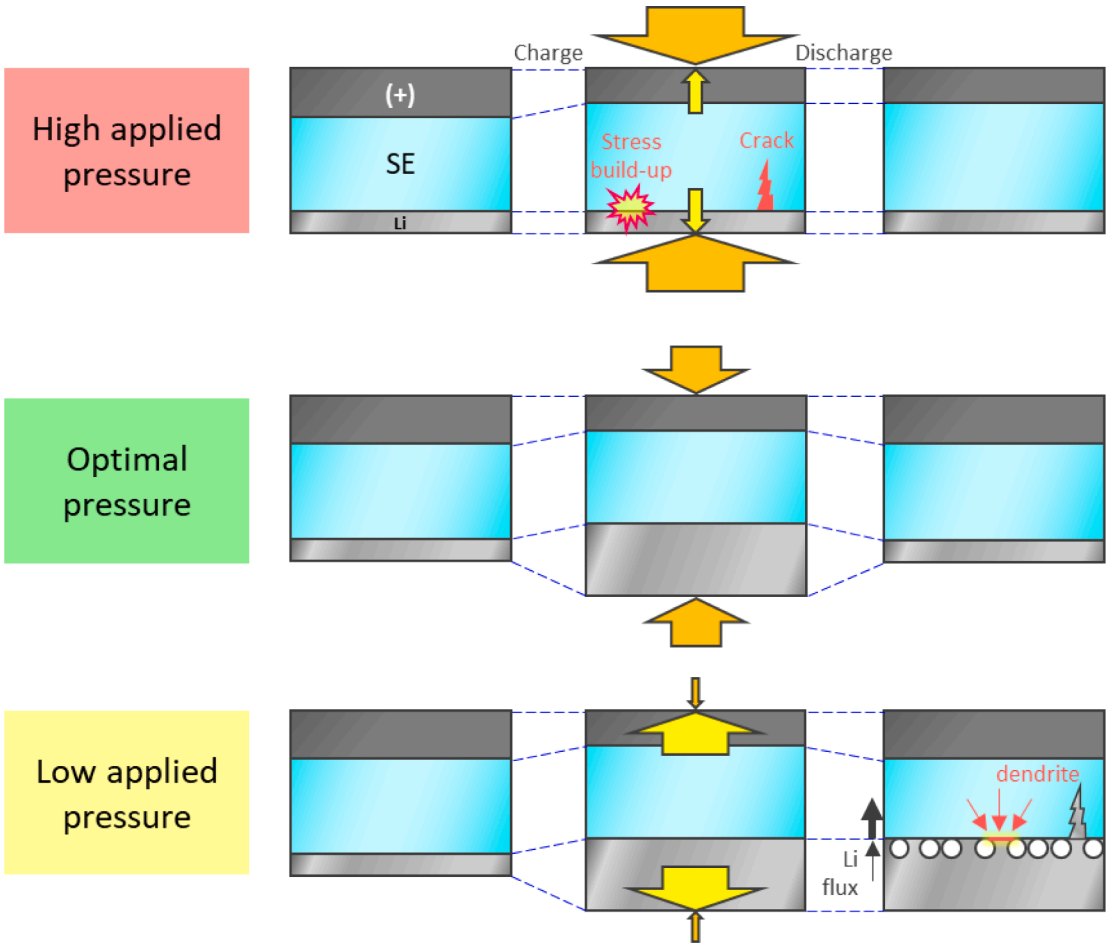

Fig. 9. Schematics illustrating the dimensional changes for ASSB cells according to externally applied pressure.

stress evolution during cycling is inevitable when exploiting state-of-the-art CAMs. Nonetheless, the stress change of the cathode ($\Delta P_{cathode}$) could be controlled by blending different CAMs. As shown in Fig. 10e, the stack pressure changes of LCO|LTO and NCM811/LTO cells during charging were positive and negative, respectively. By blending LCO and NCM811 in a weight ratio of 55:45, ΔP_{cat} was adjusted to be flat [42]. In addition to electrode engineering to minimize stress evolution, cell design that considers the "pressure cross-talk" between the cathode and anode will be a very important subject, which has not been studied intensively thus far. To optimize ASSB cells in terms of stack pressure change, multiple parameters such as the type and combination of cathode and anode, n/p ratio (the areal capacity ratio of negative to positive electrodes), pressure cross-talk, and the corresponding stresses that the SE layer experiences should be considered.

For the polymer-based SEs, the electrochemo-mechanical effects of Li|SE interfaces have been an important subject. After Monroe and Newman suggested the fiducial criterion that the dendritic growth is suppressed when the shear modulus of SE is greater than twice that of Li metal [60], many research works were dedicated to reinforce mechanical properties of SPEs [6]. While the resistance for cathode composites utilizing SPEs is largely affected by preparation conditions [190,191], the extent of stack pressure was critical to that for the Li|SPE interfaces in terms of micromechanics, contact area, and interfacial resistance [64,192,193].

The detection of ΔP_{stack} upon cycling can be utilized to diagnose the SOC status of full cells. Jung and co-workers demonstrated that *operando* DEP could precisely estimate the SOCs of NCM|graphite full cells [45]. To validate the translation of the stack pressure change into SOC, the *operando* load-measuring system was combined with all-solid-state three-electrode cells. Fig. 11a–c show the voltage profiles and pressure changes (ΔP_{Gr}) of NCM|graphite cells with different n/p ratios. ΔP_{Gr} was estimated by subtracting the stack pressure change of the NCM|LTO cell from that of the NCM|Gr cell ($\Delta P_{Gr} = \Delta P_{NCM|Gr} - \Delta P_{NCM|LTO}$). During charge, the local minimum point for the dP_{Gr}/dt vs. time curve is denoted by red markers in Fig. 11a–c for each n/p ratio. Singular points were also observed during discharge as local maxima in the DEP plot. It is noted that the local minimum points underwent a positive shift in the *x*-axis as the n/p ratio increased, reflecting larger initial irreversible capacities. In contrast, the local minima and maxima could be exploited as a milestone for tracking the SOC, which was verified by matching the actual SOC with these singular points (Fig. 11d–f). This non-destructive diagnostic technique may benefit the development of practical battery management systems for ASSBs.

5.2. *Mild-pressure operation: charge transport in electrodes*

In composite electrodes using LEs, Li^+ transport behavior is not sensitive to external pressure because of the fluidity of the LEs. In addition, a substantial amount of carbon additives can be added (if necessary) without disturbing the Li^+ pathways, removing the need for strong external pressurization. For composite electrodes for ASSBs, the effective charge transport (Li^+ and e^-) is critically affected by the level of external pressure. The types of Li^+ transport in composite electrodes include long-range ion conduction along the SE particles and charge transfer at the CAM/SE interfaces. The former is strongly affected by the initial electrode forming pressure, whereas the latter is in a dynamic situation upon cycling as the volume of active materials keeps changing. Because carbon additives block Li^+ transport, the amounts used are

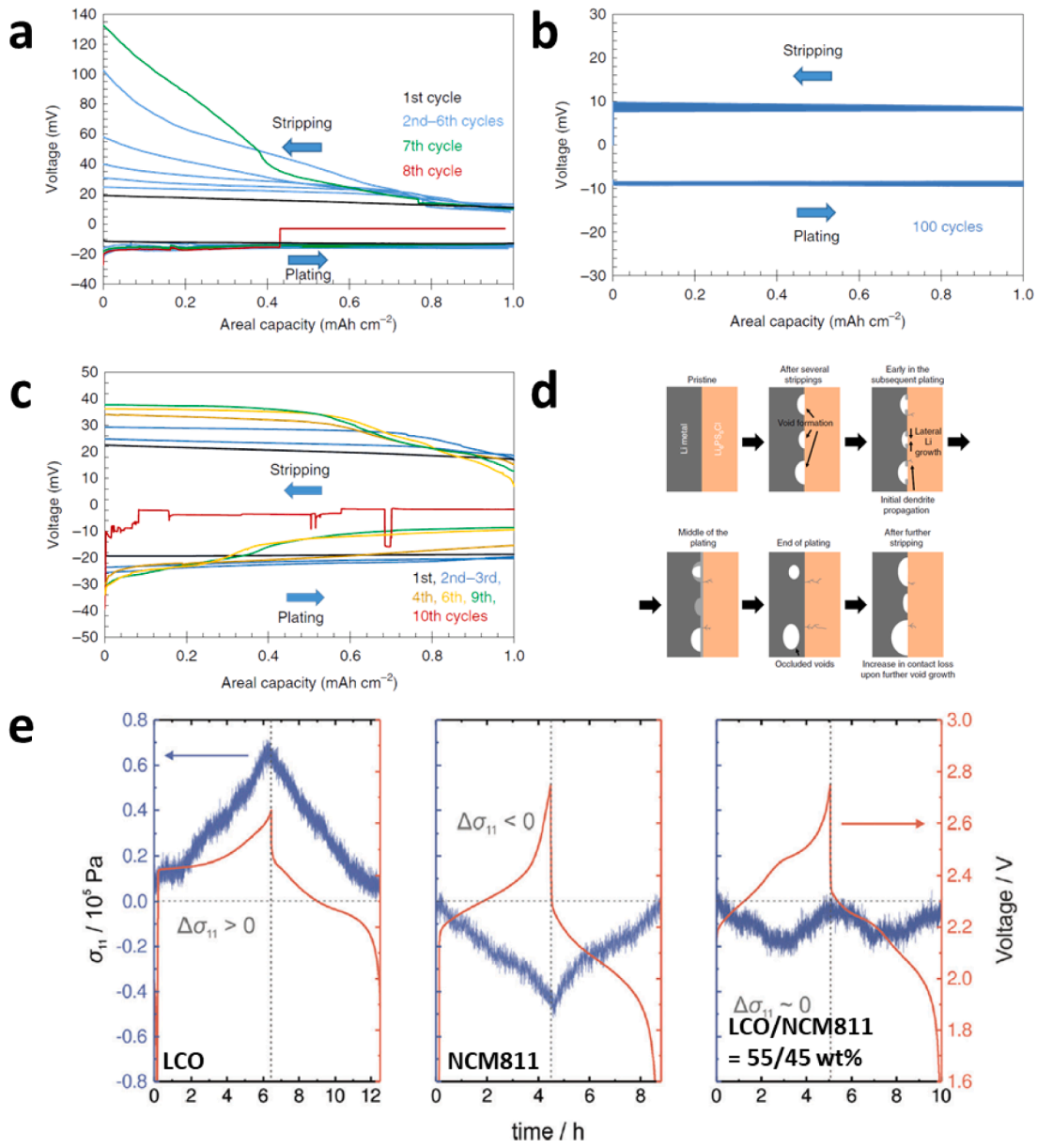

Fig. 10. Voltage profiles of Li metal upon repeated Li plating/stripping measured using three-electrode cells at a current density and applied pressure of (a) 1 mA cm^{-2} and 3 MPa, (b) 1 mA cm^{-2} and 7 MPa, and (c) 2 mA cm^{-2} and 7 MPa. Reproduced with permission from Ref. [161]. (d) Schematic of Li|Li_6PS_5Cl interface cycled at an overall current density above the critical current density. Reproduced with permission from Ref. [161]. (e) Comparison of stack pressure evolution of CAM|SE|$Li_4Ti_5O_{12}$ cells using $LiCoO_2$, $Li[Ni_{0.8}Co_{0.1}Mn_{0.1}]O_2$, and mixture of $LiCoO_2$ and $Li[Ni_{0.8}Co_{0.1}Mn_{0.1}]O_2$. Reproduced with permission from Ref. [42].

limited. Thus, the e^- conduction pathway significantly relies on the interconnection of CAM particles, which are expected to be sensitive to external pressure considering the brittle nature of CAMs.

To quantify the charge transport behavior of composite electrodes, we measured the Li^+ and e^- conductivities of composite electrodes with different weight ratios (CAM:SE = 85:15, 70:30, and 50:50) under various external pressures (20, 7, and 3 MPa). The Li^+ and e^- conductivities of composite electrodes were measured using electronically blocking (Ti|$Li_{0.5}In$|SE|Composite|SE|$Li_{0.5}In$|Ti) and ionically blocking cells (Ti|Composite|Ti) via the DC polarization method. For all preparations, Li_6PS_5Cl ($\sigma_{Li+} = 1.9 \times 10^{-3}$ S cm^{-1} at 25 °C, $\rho = 1.87$ g cm^{-3}, LPSCl) and $Li[Ni_{0.88}Co_{0.11}Mn_{0.01}]O_2$ ($\sigma_{e-} = 4.1 \times 10^{-2}$ S cm^{-1} at 25 °C, $\rho = 4.80$ g cm^{-1}, NCM88) were used as SE and CAM, respectively. For the measurements, 150-mg composite electrodes were pressed at 370 MPa in a disc shape (diameter: 13 mm). The measurement results and calculated tortuosity factors (τ_i^2) are summarized in Table 3 (see the Supporting Information for details, Fig. S1-3). The tortuosity factor represents how the transport pathway of charge carriers deviates geometrically from the shortest travel pathway, and it is widely used for composite electrodes for both LIBs and ASSBs [194–196]. The tortuosity factor is calculated as

$$\tau_i^2 = \frac{\sigma_{i,0}}{\sigma_{i,\mathrm{comp}}}\phi_i$$

where τ_i^2 is the tortuosity factor of species i, $\sigma_{i,0}$ is the conductivity of i in SE or AM, $\sigma_{i,\mathrm{comp}}$ is the conductivity of i in a composite electrode, and ϕ_i [$=V_i/(V_{CAM} + V_{SE} + V_{void})$] is the volume fraction of i. Here, a higher τ_i^2 value means that the pathway of species i is geometrically more tortuous or discontinuous under a given condition. It is reasonable to assume that Li^+ and e^- are transported only through SE and CAM, respectively.

Fig. 12 shows the tortuosity factors for Li^+ and e^- in the NCM88/LPSCl electrodes with different weight ratios under different applied pressures. As the volume ratios of CAM were increased, τ_{Li+}^2 increased

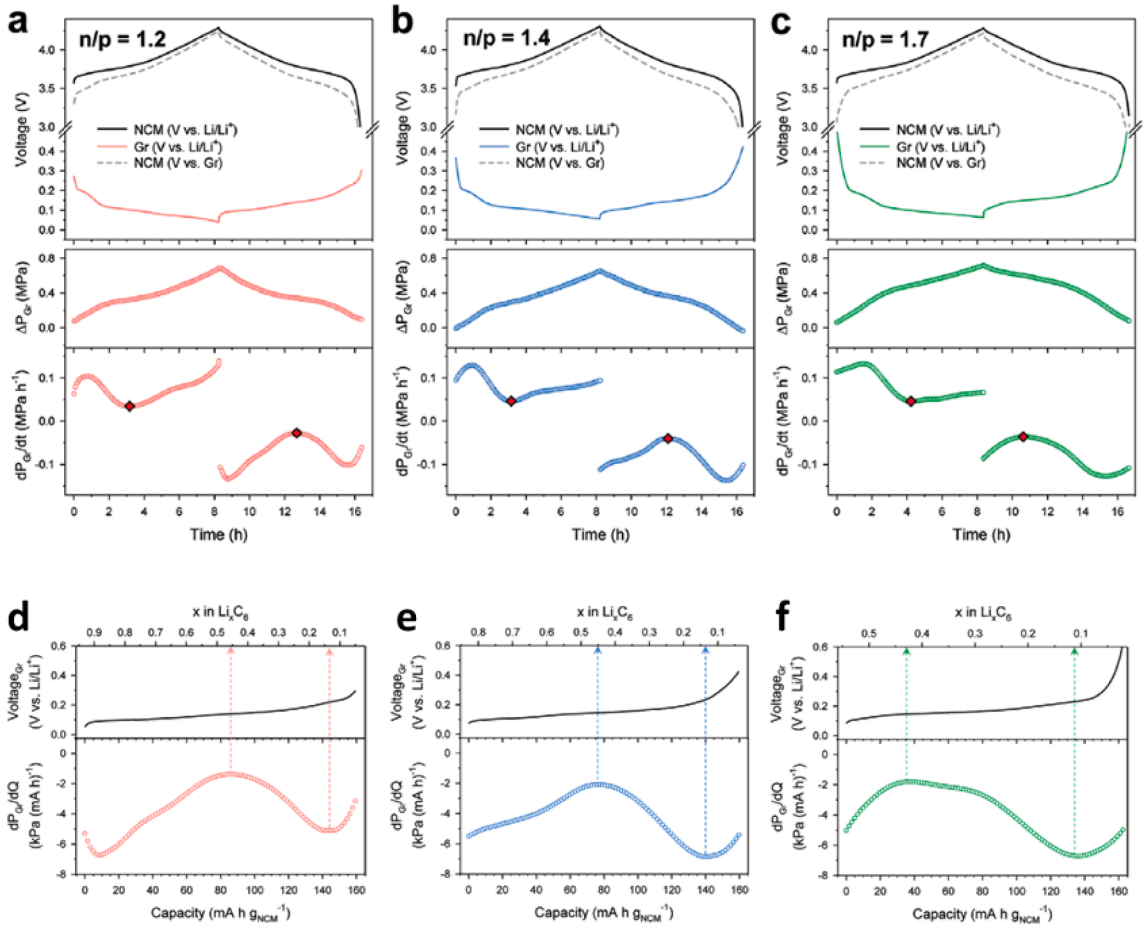

Fig. 11. DEP results of NCM/graphite full cells with n/p ratios of (a) 1.2, (b) 1.4, and (c) 1.7 at the second cycle. The cells were cycled at 0.1C and 30 °C. Reproduced with permission from Ref. [45]. The local minima and maxima are marked in red. Results of the SOC estimation by the DEP analysis for NCM|graphite full cells with n/p ratios of (d) 1.2, (e) 1.4, and (f) 1.7. Dashed vertical arrows indicate the estimated SOCs. Reproduced with permission from Ref. [45]. (For interpretation of the references to colour in this figure legend, the reader is referred to the web version of this article.)

Table 3
Measured Li^+ and e^- conductivities (σ_{Li+} and σ_{e-}) and corresponding tortuosity factors (τ^2) of composite electrodes with different ratios of NCM88 and LPSCl. The conductivity measurements were carried out by DC polarization method.

AM:SE (*wt.*)	AM:SE (*vol.*)	Pressure (MPa)	$\sigma(Li^+)$ (S cm^{-1})	$\sigma(e^-)$ (S cm^{-1})	τ^2 (Li^+)	τ^2 (e^-)
85:15	68.8:31.2	20	2.7×10^{-5}	1.9×10^{-3}	14.40	9.82
85:15	68.8:31.2	7	2.7×10^{-5}	9.1×10^{-4}	14.32	20.30
85:15	68.8:31.2	3	2.7×10^{-5}	6.4×10^{-4}	14.39	28.79
70:30	47.6:52.4	20	1.8×10^{-4}	5.1×10^{-4}	4.26	29.54
70:30	47.6:52.4	7	1.7×10^{-4}	2.4×10^{-4}	4.54	62.81
70:30	47.6:52.4	3	1.5×10^{-4}	1.2×10^{-4}	5.13	121.27
50:50	28.0:72.0	20	4.1×10^{-4}	1.5×10^{-5}	2.08	466.54
50:50	28.0:72.0	7	3.9×10^{-4}	8.8×10^{-6}	2.18	816.04
50:50	28.0:72.0	3	3.6×10^{-4}	3.6×10^{-6}	2.36	1975.79

and $\tau_{e-}{}^2$ decreased for all applied pressures (20, 7, and 3 MPa), which is explained by the increased transport volume for e^- (i.e., CAM). At a volume ratio of CAM:SE = 48:52 (equivalent to CAM:SE = 70:30 in wt. %), $\tau_{e-}{}^2$ (20 MPa: 121.3, 7 MPa: 62.8, and 3 MPa: 29.5) were much higher than $\tau_{Li+}{}^2$ (20 MPa: 5.1, 7 MPa: 4.5, and 3 MPa: 4.3). In other words, $\tau_{e-}{}^2$ was much higher than $\tau_{Li+}{}^2$ for similar volume fractions of CAM and SE. This feature reflects the different mechanical properties of the oxide CAM and sulfide SE. Interestingly, $\tau_{e-}{}^2$ was far more sensitive to external pressure than $\tau_{Li+}{}^2$. For example, for the weight ratio of CAM:SE = 85:15, the $\tau_{e-}{}^2$ values at 20, 7, and 3 MPa were 9.8, 20.3, and 28.8, respectively, whereas those of $\tau_{Li+}{}^2$ at 20, 7, and 3 MPa were 14.4, 14.3, and 14.4, respectively, and thus very similar. This result implies that the CAM/CAM contacts loosened easily under mild pressurization. The brittle nature of the oxide CAM is responsible for this contact loosening. Considering that an increased volumetric ratio of CAM and a minimized amount of carbon additive are required for composite electrodes, this concern would be challenging, but it should be resolved for ASSBs working under realistic operating conditions (e.g., <1 MPa).

6. Conclusions and outlook

In summary, the mechanical properties of SEs, the sources of internal stress generation in ASSBs, and their electrochemo-mechanical impacts on each component of ASSBs were hierarchically reviewed with the focus on using inorganic SEs. Despite the ductility of sulfide or halide SEs, their inelasticity is not fully compliant with internal stress evolution, causing several electrochemo-mechanical failures, such as CAM/SE detachment, isolation of CAM primary particles, and challenges for stack pressure, which are much more complex than those discussed herein. Because we ruled out the addition of liquids or elastic components as an ultimate solution to resolve the electrochemo-mechanical concerns in

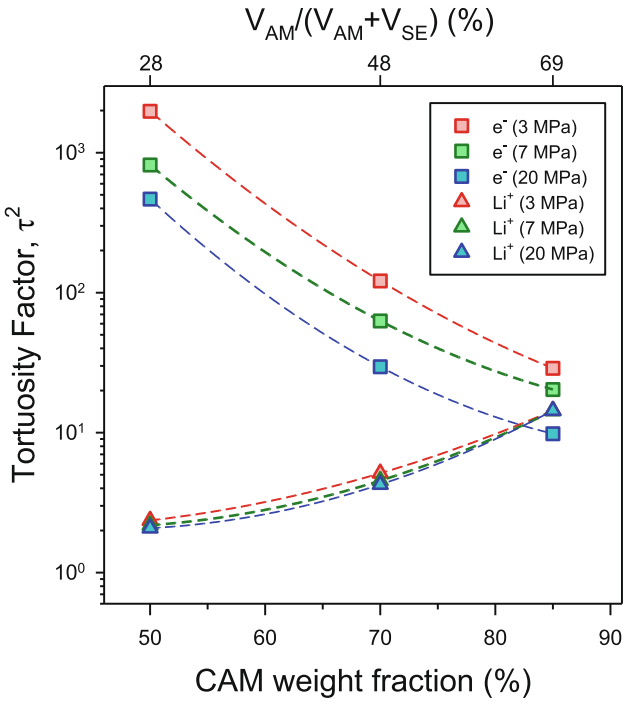

Fig. 12. Tortuosity factors (τ^2) for e^- and Li^+ conductivities of composite electrodes prepared by mixing NCM88 and LPSCl with weight ratios of 50:50, 70:30, and 85:15. For the calculation, the Li^+ and e^- conductivities of composites were measured by DC polarization method using Ti|$Li_{0.5}In$|SE|Composite|SE|$Li_{0.5}In$|Ti and Ti|Composite|Ti cells, respectively, under applied pressures of 20, 7, and 3 MPa.

this paper, the importance of CAM engineering and searching for new inorganic SEs with wide electrochemical stability windows were highlighted. In addition to material engineering, the interaction between external pressure and internal stress and the challenges of mild-pressure operation were discussed. We suggest searching for novel CAMs with more mechanical compliance and electrode engineering, such as binder/carbon optimization, as important subjects for future research. Such solutions can confer elastic mechanical properties to composite electrodes and mitigate electrochemo-mechanical failures. A plausible large-scale fabrication method for ASSBs using inorganic SEs, other than the isostatic press technique, is also indispensable for commercialization, in which the mechanical properties of the electrodes and separators are important parameters. Overall, despite the recent achievements of ASSBs, in terms of SE materials, protective coating layers, electrode optimization, understanding the electrochemo-mechanical behavior in ASSBs and enabling state-of-the-art ASSB performance under realistic operating conditions will be a formidable challenge. We hope that this paper spurs more intensive studies on this subject.

Declaration of Competing Interest

The authors declare that they have no known competing financial interests or personal relationships that could have appeared to influence the work reported in this paper.

Acknowledgement

This work was supported by the Technology Development Program to Solve Climate Changes of the National (NRF) funded by the Ministry of Science & ICT (NRF-2017M1A2A2044501) and the Creative Materials Discovery Program of the NRF funded by the Ministry of Science & ICT (NRF-2018M3D1A1058727), and by the Technology Innovation Program (20007045 and 20012216) funded By the Ministry of Trade, Industry & Energy (MOTIE, Korea). This work was also funded by the Yonsei University Research Fund of 2021 (2021-22-0326).

Notes

The authors declare no competing financial interest.

Appendix A. Supplementary material

Supplementary data to this article can be found online at https://doi.org/10.1016/j.cossms.2021.100977.

References

[1] K. Xu, Nonaqueous liquid electrolytes for lithium-based rechargeable batteries, Chem. Rev. 104 (10) (2004) 4303–4418.
[2] A. Manthiram, X. Yu, S. Wang, Lithium battery chemistries enabled by solid-state electrolytes, Nat. Rev. Mater. 2 (4) (2017) 16103.
[3] K. Kerman, A. Luntz, V. Viswanathan, Y.-M. Chiang, Z. Chen, Review—practical challenges hindering the development of solid state Li ion batteries, J. Electrochem. Soc. 164 (7) (2017) A1731–A1744.
[4] Z. Zhang, Y. Shao, B. Lotsch, Y.-S. Hu, H. Li, J. Janek, L.F. Nazar, C.-W. Nan, J. Maier, M. Armand, L. Chen, New horizons for inorganic solid state ion conductors, Energy Environ. Sci. 11 (8) (2018) 1945–1976.
[5] K.H. Park, Q. Bai, D.H. Kim, D.Y. Oh, Y. Zhu, Y. Mo, Y.S. Jung, Design strategies, practical considerations, and new solution processes of sulfide solid electrolytes for all-solid-state batteries, Adv. Energy Mater. 8 (18) (2018) 1800035.
[6] D. Zhou, D. Shanmukaraj, A. Tkacheva, M. Armand, G. Wang, Polymer electrolytes for lithium-based batteries: advances and prospects, Chem 5 (9) (2019) 2326–2352.
[7] R. Chen, Q. Li, X. Yu, L. Chen, H. Li, Approaching practically accessible solid-state batteries: stability issues related to solid electrolytes and interfaces, Chem. Rev. 120 (14) (2020) 6820–6877.
[8] Y.-G. Lee, S. Fujiki, C. Jung, N. Suzuki, N. Yashiro, R. Omoda, D.-S. Ko, T. Shiratsuchi, T. Sugimoto, S. Ryu, J.H. Ku, T. Watanabe, Y. Park, Y. Aihara, D. Im, I.T. Han, High-energy long-cycling all-solid-state lithium metal batteries enabled by silver–carbon composite anodes, Nat. Energy 5 (4) (2020) 299–308.
[9] K.T. Kim, D.Y. Oh, S. Jun, Y.B. Song, T.Y. Kwon, Y. Han, Y.S. Jung, Tailoring slurries using cosolvents and li salt targeting practical all-solid-state batteries employing sulfide solid electrolytes, Adv. Energy Mater. 11 (17) (2021) 2003766.
[10] D.Y. Oh, K.T. Kim, S.H. Jung, D.H. Kim, S. Jun, S. Jeoung, H.R. Moon, Y.S. Jung, Tactical hybrids of Li^+-conductive dry polymer electrolytes with sulfide solid electrolytes: toward practical all-solid-state batteries with wider temperature operability, Mater. Today (2021), https://doi.org/10.1016/j.mattod.2021.01.006.
[11] Y. Seino, T. Ota, K. Takada, A. Hayashi, M. Tatsumisago, A sulphide lithium super ion conductor is superior to liquid ion conductors for use in rechargeable batteries, Energy Environ. Sci. 7 (2) (2014) 627–631.
[12] N. Kamaya, K. Homma, Y. Yamakawa, M. Hirayama, R. Kanno, M. Yonemura, T. Kamiyama, Y. Kato, S. Hama, K. Kawamoto, A. Mitsui, A lithium superionic conductor, Nat. Mater. 10 (9) (2011) 682–686.
[13] Y. Kato, S. Hori, T. Saito, K. Suzuki, M. Hirayama, A. Mitsui, M. Yonemura, H. Iba, R. Kanno, High-power all-solid-state batteries using sulfide superionic conductors, Nat. Energy 1 (4) (2016) 16030.
[14] H.-J. Deiseroth, S.-T. Kong, H. Eckert, J. Vannahme, C. Reiner, T. Zaiss, M. Schlosser, Li_6PS_5X: A class of crystalline Li-rich solids with an unusually high Li^+ mobility, Ang. Chem. Int. Ed. 120 (4) (2008) 767–770.
[15] P. Adeli, J.D. Bazak, K.H. Park, I. Kochetkov, A. Huq, G.R. Goward, L.F. Nazar, Boosting solid-state diffusivity and conductivity in lithium superionic argyrodites by halide substitution, Ang. Chem. Int. Ed. 131 (26) (2019) 8773–8778.
[16] N.J.J. de Klerk, I. Rosłoń, M. Wagemaker, Diffusion mechanism of Li argyrodite solid electrolytes for Li-ion batteries and prediction of optimized halogen doping: the effect of li vacancies, halogens, and halogen disorder, Chem. Mater. 28 (21) (2016) 7955–7963.
[17] M.A. Kraft, S.P. Culver, M. Calderon, F. Böcher, T. Krauskopf, A. Senyshyn, C. Dietrich, A. Zevalkink, J. Janek, W.G. Zeier, Influence of lattice polarizability on the ionic conductivity in the lithium superionic argyrodites Li_6PS_5X (X = Cl, Br, I), J. Am. Chem. Soc. 139 (31) (2017) 10909–10918.
[18] D.H. Kim, D.Y. Oh, K.H. Park, Y.E. Choi, Y.J. Nam, H.A. Lee, S.-M. Lee, Y.S. Jung, Infiltration of solution-processable solid electrolytes into conventional Li-ion-battery electrodes for all-solid-state Li-ion batteries, Nano Lett. 17 (5) (2017) 3013–3020.
[19] Y.B. Song, D.H. Kim, H. Kwak, D. Han, S. Kang, J.H. Lee, S.-M. Bak, K.-W. Nam, H.-W. Lee, Y.S. Jung, Tailoring solution-processable Li argyrodites $Li_{6+x}P_{1-x}M_xS_5I$ (M= Ge, Sn) and their microstructural evolution revealed by Cryo-TEM for all-solid-state batteries, Nano Lett. 20 (6) (2020) 4337–4345.
[20] D.H. Kim, Y.-H. Lee, Y.B. Song, H. Kwak, S.-Y. Lee, Y.S. Jung, Thin and flexible solid electrolyte membranes with ultrahigh thermal stability derived from solution-processable Li argyrodites for all-solid-state Li-ion batteries, ACS Energy Letters 5 (3) (2020) 718–727.
[21] W.D. Richards, L.J. Miara, Y. Wang, J.C. Kim, G. Ceder, Interface stability in solid-state batteries, Chem. Mater. 28 (1) (2016) 266–273.

[22] Y. Zhu, X. He, Y. Mo, First principles study on electrochemical and chemical stability of solid electrolyte–electrode interfaces in all-solid-state Li-ion batteries, J. Mater. Chem. A 4 (9) (2016) 3253–3266.

[23] S. Wang, Q. Bai, A.M. Nolan, Y. Liu, S. Gong, Q. Sun, Y. Mo, Lithium chlorides and bromides as promising solid-state chemistries for fast ion conductors with good electrochemical stability, Ang. Chem. Int. Ed. 58 (24) (2019) 8039–8043.

[24] N. Ohta, K. Takada, I. Sakaguchi, L. Zhang, R. Ma, K. Fukuda, M. Osada, T. Sasaki, $LiNbO_3$-coated $LiCoO_2$ as cathode material for all solid-state lithium secondary batteries, Electrochem. Commun. 9 (7) (2007) 1486–1490.

[25] S. Ito, S. Fujiki, T. Yamada, Y. Aihara, Y. Park, T.Y. Kim, S.-W. Baek, J.-M. Lee, S. Doo, N. Machida, A rocking chair type all-solid-state lithium ion battery adopting Li_2O–ZrO_2 coated $LiNi_{0.8}Co_{0.15}Al_{0.05}O_2$ and a sulfide based electrolyte, J. Power Sources 248 (2014) 943–950.

[26] S.H. Jung, K. Oh, Y.J. Nam, D.Y. Oh, P. Brüner, K. Kang, Y.S. Jung, Li_3BO_3–Li_2CO_3: rationally designed buffering phase for sulfide all-solid-state Li-ion batteries, Chem. Mater. 30 (22) (2018) 8190–8200.

[27] T. Asano, A. Sakai, S. Ouchi, M. Sakaida, A. Miyazaki, S. Hasegawa, Solid Halide electrolytes with high lithium-ion conductivity for application in 4 V class bulk-type all-solid-state batteries, Adv. Mater. 30 (44) (2018) 1803075.

[28] X. Li, J. Liang, J. Luo, M. Norouzi Banis, C. Wang, W. Li, S. Deng, C. Yu, F. Zhao, Y. Hu, T.-K. Sham, L. Zhang, S. Zhao, S. Lu, H. Huang, R. Li, K.R. Adair, X. Sun, Air-stable Li_3InCl_6 electrolyte with high voltage compatibility for all-solid-state batteries, Energy Environ. Sci. 12 (9) (2019) 2665–2671.

[29] L. Zhou, C.Y. Kwok, A. Shyamsunder, Q. Zhang, X. Wu, L.F. Nazar, A new halospinel superionic conductor for high-voltage all solid state lithium batteries, Energy Environ. Sci. 13 (7) (2020) 2056–2063.

[30] X. Li, J. Liang, K.R. Adair, J. Li, W. Li, F. Zhao, Y. Hu, T.-K. Sham, L. Zhang, S. Zhao, S. Lu, H. Huang, R. Li, N. Chen, X. Sun, Origin of superionic $Li_3Y_{1-x}In_xCl_6$ halide solid electrolytes with high humidity tolerance, Nano Lett. 20 (6) (2020) 4384–4392.

[31] K.-H. Park, K. Kaup, A. Assoud, Q. Zhang, X. Wu, L.F. Nazar, High-voltage superionic halide solid electrolytes for all-solid-state Li-ion batteries, ACS Energy Lett. 5 (2) (2020) 533–539.

[32] J. Park, D. Han, H. Kwak, Y. Han, Y.J. Choi, K.-W. Nam, Y.S. Jung, Heat treatment protocol for modulating ionic conductivity via structural evolution of $Li_{3-x}Yb_{1-x}M_xCl_6$ ($M = Hf^{4+}$, Zr^{4+}) new halide superionic conductors for all-solid-state batteries, Chem. Eng. J. 425 (2021), 130630.

[33] H. Kwak, D. Han, J. Lyoo, J. Park, S.H. Jung, Y. Han, G. Kwon, H. Kim, S.-T. Hong, K.-W. Nam, Y.S. Jung, New cost-effective halide solid electrolytes for all-solid-state batteries: mechanochemically prepared Fe^{3+}-substituted Li_2ZrCl_6, Adv. Energy Mater. 11 (12) (2021) 2003190.

[34] H. Kwak, J. Lyoo, J. Park, Y. Han, R. Asakura, A. Remhof, C. Battaglia, H. Kim, S.-T. Hong, Y.S. Jung, Na_2ZrCl_6 enabling highly stable 3 V all-solid-state Na-ion batteries, Energy Storage Mater. 37 (2021) 47–54.

[35] H. Maekawa, M. Matsuo, H. Takamura, M. Ando, Y. Noda, T. Karahashi, S.-I. Orimo, Halide-stabilized $LiBH_4$, a room-temperature lithium fast-ion conductor, J. Am. Chem. Soc. 131 (3) (2009) 894–895.

[36] S. Kim, H. Oguchi, N. Toyama, T. Sato, S. Takagi, T. Otomo, D. Arunkumar, N. Kuwata, J. Kawamura, S.-I. Orimo, A complex hydride lithium superionic conductor for high-energy-density all-solid-state lithium metal batteries, Nat. Commun. 10 (1) (2019) 1081.

[37] M. Kotobuki, M. Koishi, Preparation of $Li_7La_3Zr_2O_{12}$ solid electrolyte via a sol–gel method, Ceram. Int. 40 (3) (2014) 5043–5047.

[38] Y. Kato, S. Shiotani, K. Morita, K. Suzuki, M. Hirayama, R. Kanno, All-solid-state batteries with thick electrode configurations, J. Phys. Chem. Lett. 9 (3) (2018) 607–613.

[39] D.Y. Oh, Y.J. Nam, K.H. Park, S.H. Jung, K.T. Kim, A.R. Ha, Y.S. Jung, Slurry-fabricable Li^+-conductive polymeric binders for practical all-solid-state lithium-ion batteries enabled by solvate ionic liquids, Adv. Energy Mater. 9 (16) (2019) 1802927.

[40] F. Hippauf, B. Schumm, S. Doerfler, H. Althues, S. Fujiki, T. Shiratsuchi, T. Tsujimura, Y. Aihara, S. Kaskel, Overcoming binder limitations of sheet-type solid-state cathodes using a solvent-free dry-film approach, Energy Storage Mater. 21 (2019) 390–398.

[41] F.P. McGrogan, T. Swamy, S.R. Bishop, E. Eggleton, L. Porz, X. Chen, Y.-M. Chiang, K.J. Van Vliet, Compliant yet brittle mechanical behavior of Li_2S–P_2S_5 lithium-ion-conducting solid electrolyte, Adv. Energy Mater. 7 (12) (2017) 1602011.

[42] R. Koerver, W. Zhang, L. de Biasi, S. Schweidler, A.O. Kondrakov, S. Kolling, T. Brezesinski, P. Hartmann, W.G. Zeier, J. Janek, Chemo-mechanical expansion of lithium electrode materials – on the route to mechanically optimized all-solid-state batteries, Energy Environ. Sci. 11 (8) (2018) 2142–2158.

[43] S. Wang, W. Zhang, X. Chen, D. Das, R. Ruess, A. Gautam, F. Walther, S. Ohno, R. Koerver, Q. Zhang, W.G. Zeier, F.H. Richter, C.-W. Nan, J. Janek, Influence of crystallinity of lithium thiophosphate solid electrolytes on the performance of solid-state batteries, Adv. Energy Mater. 11 (2021) 2100654.

[44] S.H. Jung, U.-H. Kim, J.-H. Kim, S. Jun, C.S. Yoon, Y.S. Jung, Y.-K. Sun, Ni-rich layered cathode materials with electrochemo-mechanically compliant microstructures for all-solid-state Li batteries, Adv. Energy Mater. 10 (6) (2020) 1903360.

[45] S. Jun, Y.J. Nam, H. Kwak, K.T. Kim, D.Y. Oh, Y.S. Jung, Operando differential electrochemical pressiometry for probing electrochemo-mechanics in all-solid-state batteries, Adv. Funct. Mater. 30 (31) (2020) 2002535.

[46] Y. Han, S.H. Jung, H. Kwak, S. Jun, H.H. Kwak, J.H. Lee, S.-T. Hong, Y.S. Jung, Single- or poly-crystalline Ni-rich layered cathode, sulfide or halide solid electrolyte: which will be the winners for all-solid-state batteries? Adv. Energy Mater. 11 (21) (2021) 2100126.

[47] R. Ruess, S. Schweidler, H. Hemmelmann, G. Conforto, A. Bielefeld, D.A. Weber, J. Sann, M.T. Elm, J. Janek, Influence of NCM particle cracking on kinetics of lithium-ion batteries with liquid or solid electrolyte, J. Electrochem. Soc. 167 (10) (2020), 100532.

[48] S. Oswald, D. Pritzl, M. Wetjen, H.A. Gasteiger, Novel method for monitoring the electrochemical capacitance by in situ impedance spectroscopy as indicator for particle cracking of nickel-rich NCMs: Part I. theory and validation, J. Electrochem. Soc. 167 (10) (2020), 100511.

[49] F. Friedrich, B. Strehle, A.T.S. Freiberg, K. Kleiner, S.J. Day, C. Erk, M. Piana, H. A. Gasteiger, Editors' choice—capacity fading mechanisms of NCM-811 cathodes in lithium-ion batteries studied by X-ray diffraction and other diagnostics, J. Electrochem. Soc. 166 (15) (2019) A3760–A3774.

[50] R. Koerver, I. Aygün, T. Leichtweiß, C. Dietrich, W. Zhang, J.O. Binder, P. Hartmann, W.G. Zeier, J. Janek, Capacity fade in solid-state batteries: interphase formation and chemomechanical processes in nickel-rich layered oxide cathodes and lithium thiophosphate solid electrolytes, Chem. Mater. 29 (13) (2017) 5574–5582.

[51] T. Krauskopf, H. Hartmann, W.G. Zeier, J. Janek, Toward a fundamental understanding of the lithium metal anode in solid-state batteries—an electrochemo-mechanical study on the garnet-type solid electrolyte $Li_{6.25}Al_{0.25}La_3Zr_2O_{12}$, ACS Appl Mater. Interfaces 11 (15) (2019) 14463–14477.

[52] J. Dai, C. Yang, C. Wang, G. Pastel, L. Hu, Interface engineering for garnet-based solid-state lithium-metal batteries: materials, structures, and characterization, Adv. Mater. 30 (48) (2018) 1802068.

[53] D. Wang, C. Zhu, Y. Fu, X. Sun, Y. Yang, Interfaces in garnet-based all-solid-state lithium batteries, Adv. Energy Mater. 10 (39) (2020) 2001318.

[54] A.L. Davis, R. Garcia-Mendez, K.N. Wood, E. Kazyak, K.-H. Chen, G. Teeter, J. Sakamoto, N.P. Dasgupta, Electro-chemo-mechanical evolution of sulfide solid electrolyte/Li metal interfaces: operando analysis and ALD interlayer effects, J. Mater. Chem. A 8 (13) (2020) 6291–6302.

[55] C. Wang, J. Liang, Y. Zhao, M. Zheng, X. Li, X. Sun, All-solid-state lithium batteries enabled by sulfide electrolytes: from fundamental research to practical engineering design, Energy Environ. Sci. 14 (5) (2021) 2577–2619.

[56] W.S. LePage, Y. Chen, E. Kazyak, K.-H. Chen, A.J. Sanchez, A. Poli, E.M. Arruda, M.D. Thouless, N.P. Dasgupta, Lithium mechanics: roles of strain rate and temperature and implications for lithium metal batteries, J. Electrochem. Soc. 166 (2) (2019) A89–A97.

[57] L. Long, S. Wang, M. Xiao, Y. Meng, Polymer electrolytes for lithium polymer batteries, J. Mater. Chem. A 4 (26) (2016) 10038–10069.

[58] S. Tang, W. Guo, Y. Fu, Advances in composite polymer electrolytes for lithium batteries and beyond, Adv. Energy Mater. 11 (2) (2021) 2000802.

[59] A.A. Rulev, Y.O. Kondratyeva, L.V. Yashina, D.M. Itkis, Lithium planar deposition vs whisker growth: crucial role of surface diffusion, J. Phys. Chem. Lett. 11 (24) (2020) 10511–10518.

[60] C. Monroe, J. Newman, The impact of elastic deformation on deposition kinetics at lithium/polymer interfaces, J. Electrochem. Soc. 152 (2) (2005) A396.

[61] L. Porz, T. Swamy, B.W. Sheldon, D. Rettenwander, T. Frömling, H.L. Thaman, S. Berendts, R. Uecker, W.C. Carter, Y.-M. Chiang, Mechanism of lithium metal penetration through inorganic solid electrolytes, Adv. Energy Mater. 7 (20) (2017) 1701003.

[62] S.-H. Wang, Y.-X. Yin, T.-T. Zuo, W. Dong, J.-Y. Li, J.-L. Shi, C.-H. Zhang, N.-W. Li, C.-J. Li, Y.-G. Guo, Stable Li metal anodes via regulating lithium plating/stripping in vertically aligned microchannels, Adv. Mater. 29 (40) (2017) 1703729.

[63] X. Han, Y. Gong, K. Fu, X. He, G.T. Hitz, J. Dai, A. Pearse, B. Liu, H. Wang, G. Rubloff, Y. Mo, V. Thangadurai, E.D. Wachsman, L. Hu, Negating interfacial impedance in garnet-based solid-state Li metal batteries, Nat. Mater. 16 (5) (2017) 572–579.

[64] P. Wang, W. Qu, W.-L. Song, H. Chen, R. Chen, D. Fang, Electro–chemo–mechanical issues at the interfaces in solid-state lithium metal batteries, Adv. Funct. Mater. 29 (27) (2019) 1900950.

[65] R. Wei, S. Chen, T. Gao, W. Liu, Challenges, fabrications and horizons of oxide solid electrolytes for solid-state lithium batteries, Nano Select (2021), https://doi.org/10.1002/nano.202100110.

[66] X. Li, J. Liang, X. Yang, K.R. Adair, C. Wang, F. Zhao, X. Sun, Progress and perspectives on halide lithium conductors for all-solid-state lithium batteries, Energy Environ. Sci. 13 (5) (2020) 1429–1461.

[67] A. Sharafi, S. Yu, M. Naguib, M. Lee, C. Ma, H.M. Meyer, J. Nanda, M. Chi, D. J. Siegel, J. Sakamoto, Impact of air exposure and surface chemistry on Li–$Li_7La_3Zr_2O_{12}$ interfacial resistance, J. Mater. Chem. A 5 (26) (2017) 13475–13487.

[68] A. Banerjee, K.H. Park, J.W. Heo, Y.J. Nam, C.K. Moon, S.M. Oh, S.-T. Hong, Y. S. Jung, Na_3SbS_4: a solution processable sodium superionic conductor for all-solid-state sodium-ion batteries, Ang. Chem. Int. Ed. 128 (33) (2016) 9786–9790.

[69] K.H. Park, D.Y. Oh, Y.E. Choi, Y.J. Nam, L. Han, J.-Y. Kim, H. Xin, F. Lin, S.M. Oh, Y.S. Jung, Solution-processable glass lii-li$_4$sns$_4$ superionic conductors for all-solid-state Li-ion batteries, Adv. Mater. 28 (9) (2016) 1874–1883.

[70] J.W. Heo, A. Banerjee, K.H. Park, Y.S. Jung, S.-T. Hong, New Na-ion solid electrolytes $Na_{4-x}Sn_{1-x}Sb_xS_4$ ($0.02 \leq x \leq 0.33$) for all-solid-state Na-ion batteries, Adv. Energy Mater. 8 (11) (2018) 1702716.

[71] Y.E. Choi, K.H. Park, D.H. Kim, D.Y. Oh, H.R. Kwak, Y.-G. Lee, Y.S. Jung, Coatable Li_4SnS_4 solid electrolytes prepared from aqueous solutions for all-solid-state lithium-ion batteries, ChemSusChem 10 (12) (2017) 2605–2611.

[72] K.H. Park, D.H. Kim, H. Kwak, S.H. Jung, H.-J. Lee, A. Banerjee, J.H. Lee, Y. S. Jung, Solution-derived glass-ceramic NaI·Na_3SbS_4 superionic conductors for all-solid-state Na-ion batteries, J. Mater. Chem. A 6 (35) (2018) 17192–17200.

[73] T.W. Kim, K.H. Park, Y.E. Choi, J.Y. Lee, Y.S. Jung, Aqueous-solution synthesis of Na_3SbS_4 solid electrolytes for all-solid-state Na-ion batteries, J. Mater. Chem. A 6 (3) (2018) 840–844.

[74] H. Kwak, K.H. Park, D. Han, K.-W. Nam, H. Kim, Y.S. Jung, Li^+ conduction in air-stable Sb-substituted Li_4SnS_4 for all-solid-state Li-Ion batteries, J. Power Sources 446 (2020), 227338.

[75] D. Lee, K.-H. Park, S.Y. Kim, J.Y. Jung, W. Lee, K. Kim, G. Jeong, J.-S. Yu, J. Choi, M.-S. Park, W. Cho, Critical role of zeolites as H_2S scavengers in argyrodite Li_6PS_5Cl solid electrolytes for all-solid-state batteries, J. Mater. Chem. A 9 (32) (2021) 17311–17316.

[76] T. Ohtomo, A. Hayashi, M. Tatsumisago, K. Kawamoto, Characteristics of the Li_2O–Li_2S–P_2S_5 glasses synthesized by the two-step mechanical milling, J. Non-Cryst. Solids 364 (2013) 57–61.

[77] G. Sahu, Z. Lin, J. Li, Z. Liu, N. Dudney, C. Liang, Air-stable, high-conduction solid electrolytes of arsenic-substituted Li_4SnS_4, Energy Environ. Sci. 7 (3) (2014) 1053–1058.

[78] A. Hayashi, H. Muramatsu, T. Ohtomo, S. Hama, M. Tatsumisago, Improvement of chemical stability of Li_3PS_4 glass electrolytes by adding M_xO_y (M = Fe, Zn, and Bi) nanoparticles, J. Mater. Chem. A 1 (21) (2013) 6320–6326.

[79] X. Chen, Z. Guan, F. Chu, Z. Xue, F. Wu, Y. Yu, Air-stable inorganic solid-state electrolytes for high energy density lithium batteries: challenges, strategies, and prospects, InfoMat (2021), https://doi.org/10.1002/inf2.12248.

[80] S. Zhao, X. Zhu, J. Wei, Z. Ji, M. Ling, L. Wang, C. Liang, Fundamental air stability in solid-state electrolytes: principles and solutions, Mater. Chem. Front. 5 (2021) 7452–7466.

[81] S. Seki, Y. Kobayashi, H. Miyashiro, Y. Mita, T. Iwahori, Fabrication of high-voltage, high-capacity all-solid-state lithium polymer secondary batteries by application of the polymer electrolyte/inorganic electrolyte composite concept, Chem. Mater. 17 (8) (2005) 2041–2045.

[82] H. Miyashiro, Y. Kobayashi, S. Seki, Y. Mita, A. Usami, M. Nakayama, M. Wakihara, Fabrication of all-solid-state lithium polymer secondary batteries using Al_2O_3-coated $LiCoO_2$, Chem. Mater. 17 (23) (2005) 5603–5605.

[83] J. Ma, Z. Liu, B. Chen, L. Wang, L. Yue, H. Liu, J. Zhang, Z. Liu, G. Cui, A Strategy to make high voltage $LiCoO_2$ compatible with polyethylene oxide electrolyte in all-solid-state lithium ion batteries, J. Electrochem. Soc. 164 (14) (2017) A3454–A3461.

[84] B.R. Shin, Y.J. Nam, D.Y. Oh, D.H. Kim, J.W. Kim, Y.S. Jung, Comparative study of TiS_2/Li-in all-solid-state lithium batteries using glass-ceramic Li_3PS_4 and $Li_{10}GeP_2S_{12}$ solid electrolytes, Electrochim. Acta 146 (2014) 395–402.

[85] J. Liu, S. Wang, Y. Qie, Q. Sun, Identifying lithium fluorides for promising solid-state electrolyte and coating material of high-voltage cathode, Mater. Today Energy 21 (2021), 100719.

[86] S. Wenzel, T. Leichtweiss, D.A. Weber, J. Sann, W.G. Zeier, J. Janek, Interfacial reactivity benchmarking of the sodium ion conductors Na_3PS_4 and sodium β-alumina for protected sodium metal anodes and sodium all-solid-state batteries, ACS Appl. Mater. Interfaces 8 (41) (2016) 28216–28224.

[87] J. Cho, Q. Li, H. Wang, Z. Fan, J. Li, S. Xue, K.S.N. Vikrant, H. Wang, T.B. Holland, A.K. Mukherjee, R.E. García, X. Zhang, High temperature deformability of ductile flash-sintered ceramics via in-situ compression, Nat. Commun. 9 (1) (2018) 2063.

[88] T. Woignier, J. Primera, A. Alaoui, P. Etienne, F. Despestis, S. Calas-Etienne, Mechanical properties and brittle behavior of silica aerogels, Gels 1 (2) (2015) 256–275.

[89] Y. Estrin, 2 - Dislocation-Density–Related Constitutive Modeling, in: A.S. Krausz, K. Krausz (Eds.), Unified Constitutive Laws of Plastic Deformation, Academic Press, San Diego, 1996, pp. 69–106.

[90] H.S. Kim, M.B. Bush, The effects of grain size and porosity on the elastic modulus of nanocrystalline materials, Nanostruct. Mater. 11 (3) (1999) 361–367.

[91] L.L. Baranowski, C.M. Heveran, V.L. Ferguson, C.R. Stoldt, Multi-scale mechanical behavior of the Li_3PS_4 solid-phase electrolyte, ACS Appl. Mater. Interfaces 8 (43) (2016) 29573–29579.

[92] A. Kato, M. Yamamoto, A. Sakuda, A. Hayashi, M. Tatsumisago, Mechanical properties of Li_2S–P_2S_5 glasses with lithium halides and application in all-solid-state batteries, ACS Appl. Energy Mater. 1 (3) (2018) 1002–1007.

[93] R. Garcia-Mendez, J.G. Smith, J.C. Neuefeind, D.J. Siegel, J. Sakamoto, Correlating macro and atomic structure with elastic properties and ionic transport of glassy Li_2S-P_2S_5 (LPS) solid electrolyte for solid-state Li metal batteries, Adv. Energy Mater. 10 (19) (2020) 2000335.

[94] J.E. Ni, E.D. Case, J.S. Sakamoto, E. Rangasamy, J.B. Wolfenstine, Room temperature elastic moduli and Vickers hardness of hot-pressed LLZO cubic garnet, J. Mater. Sci. 47 (23) (2012) 7978–7985.

[95] Z. Deng, Z. Wang, I.-H. Chu, J. Luo, S.P. Ong, Elastic properties of alkali superionic conductor electrolytes from first principles calculations, J. Electrochem. Soc. 163 (2) (2015) A67–A74.

[96] S. Yu, R.D. Schmidt, R. Garcia-Mendez, E. Herbert, N.J. Dudney, J.B. Wolfenstine, J. Sakamoto, D.J. Siegel, Elastic properties of the solid electrolyte $Li_7La_3Zr_2O_{12}$ (LLZO), Chem. Mater. 28 (1) (2016) 197–206.

[97] M. Jiang, S. Mukherjee, Z.W. Chen, L.X. Chen, M.L. Li, H.Y. Xiao, C. Gao, C. V. Singh, Materials perspective on new lithium chlorides and bromides: insights into thermo-physical properties, Phys. Chem. Chem. Phys. 22 (39) (2020) 22758–22767.

[98] K. Nagao, M. Suyama, A. Kato, C. Hotehama, M. Deguchi, A. Sakuda, A. Hayashi, M. Tatsumisago, Highly stable Li/Li_3BO_3–Li_2SO_4 interface and application to bulk-type all-solid-state lithium metal batteries, ACS Appl. Energy Mater. 2 (5) (2019) 3042–3048.

[99] H. Nagata, J. Akimoto, Excellent deformable oxide glass electrolytes and oxide-type all-solid-state Li_2S–Si batteries employing these electrolytes, ACS Appl. Mater. Interfaces 13 (20) (2021) 35785–35794.

[100] A. Sakuda, A. Hayashi, M. Tatsumisago, Sulfide solid electrolyte with favorable mechanical property for all-solid-state lithium battery, Sci. Rep. 3 (1) (2013) 2261.

[101] Y. Yang, Q. Wu, Y. Cui, Y. Chen, S. Shi, R.-Z. Wang, H. Yan, Elastic properties, defect thermodynamics, electrochemical window, phase stability, and Li^+ mobility of Li_3PS_4: insights from first-principles calculations, ACS Appl. Mater. Interfaces 8 (38) (2016) 25229–25242.

[102] S.F. Pugh, Xcii., Relations between the elastic moduli and the plastic properties of polycrystalline pure metals, London, Edinburgh, Dublin, Philos. Mag. J. Sci. 45 (367) (1954) 823–843.

[103] J. Swenson, L. Börjesson, Correlation between free volume and ionic conductivity in fast ion conducting glasses, Phys. Rev. Lett. 77 (17) (1996) 3569–3572.

[104] K.H. Kim, Y. Iriyama, K. Yamamoto, S. Kumazaki, T. Asaka, K. Tanabe, C.A. J. Fisher, T. Hirayama, R. Murugan, Z. Ogumi, Characterization of the interface between $LiCoO_2$ and $Li_7La_3Zr_2O_{12}$ in an all-solid-state rechargeable lithium battery, J. Power Sources 196 (2) (2011) 764–767.

[105] A. Patil, V. Patil, D. Wook Shin, J.-W. Choi, D.-S. Paik, S.-J. Yoon, Issue and challenges facing rechargeable thin film lithium batteries, Mater. Res. Bull. 43 (8) (2008) 1913–1942.

[106] Y. Zheng, Y. Yao, J. Ou, M. Li, D. Luo, H. Dou, Z. Li, K. Amine, A. Yu, Z. Chen, A review of composite solid-state electrolytes for lithium batteries: fundamentals, key materials and advanced structures, Chem. Soc. Rev. 49 (2020) 8790–8839.

[107] L.-Z. Fan, H. He, C.-W. Nan, Tailoring inorganic–polymer composites for the mass production of solid-state batteries, Nat. Rev. Mater. 6 (2021) 1003–1019.

[108] C. Yang, L. Zhang, B. Liu, S. Xu, T. Hamann, D. McOwen, J. Dai, W. Luo, Y. Gong, E.D. Wachsman, L. Hu, Continuous plating/stripping behavior of solid-state lithium metal anode in a 3D ion-conductive framework, Proc. Natl. Acad. Sci. U.S. A. 115 (15) (2018) 3770–3775.

[109] Y. Ren, T. Liu, Y. Shen, Y. Lin, C.-W. Nan, Garnet-type oxide electrolyte with novel porous-dense bilayer configuration for rechargeable all-solid-state lithium batteries, Ionics 23 (9) (2017) 2521–2527.

[110] E. Yi, H. Shen, S. Heywood, J. Alvarado, D.Y. Parkinson, G. Chen, S.W. Sofie, M. M. Doeff, All-solid-state batteries using rationally designed garnet electrolyte frameworks, ACS Appl. Energy Mater. 3 (1) (2020) 170–175.

[111] K.J. Kim, J.L.M. Rupp, All ceramic cathode composite design and manufacturing towards low interfacial resistance for garnet-based solid-state lithium batteries, Energy Environ. Sci. 13 (12) (2020) 4930–4945.

[112] Y. Ren, T. Liu, Y. Shen, Y. Lin, C.-W. Nan, Chemical compatibility between garnet-like solid state electrolyte $Li_{6.75}La_3Zr_{1.75}Ta_{0.25}O_{12}$ and major commercial lithium battery cathode materials, J. Materiomics 2 (3) (2016) 256–264.

[113] J. Wakasugi, H. Munakata, K. Kanamura, Thermal stability of various cathode materials against $Li_{6.25}Al_{0.25}La_3Zr_2O_{12}$ electrolyte, Electrochemistry 85 (2) (2017) 77–81.

[114] L.J. Miara, W.D. Richards, Y.E. Wang, G. Ceder, First-principles studies on cation dopants and electrolyte|cathode interphases for lithium garnets, Chem. Mater. 27 (11) (2015) 4040–4047.

[115] Y. Xiao, L.J. Miara, Y. Wang, G. Ceder, Computational screening of cathode coatings for solid-state batteries, Joule 3 (5) (2019) 1252–1275.

[116] S. Yu, A. Mertens, H. Tempel, R. Schierholz, H. Kungl, R.A. Eichel, Monolithic all-phosphate solid-state lithium-ion battery with improved interfacial compatibility, ACS Appl. Mater. Interfaces 10 (26) (2018) 22264–22277.

[117] T. Shi, Q. Tu, Y. Tian, Y. Xiao, L.J. Miara, O. Kononova, G. Ceder, High active material loading in all-solid-state battery electrode via particle size optimization, Adv. Energy Mater. 10 (1) (2020) 1902881.

[118] F. Strauss, T. Bartsch, L. de Biasi, A.Y. Kim, J. Janek, P. Hartmann, T. Brezesinski, Impact of cathode material particle size on the capacity of bulk-type all-solid-state batteries, ACS Energy Lett. 3 (4) (2018) 992–996.

[119] M. Seyedi, S. Haratian, J.V. Khaki, Mechanochemical synthesis of Fe_2O_3 nanoparticles, Proc. Mater. Sci. 11 (2015) 309–313.

[120] S. Palaniandy, K.A.M. Azizli, Mechanochemical effects on talc during fine grinding process in a jet mill, Int. J. Miner. Process. 92 (1) (2009) 22–33.

[121] Y. Koyama, T.E. Chin, U. Rhyner, R.K. Holman, S.R. Hall, Y.M. Chiang, Harnessing the actuation potential of solid-state intercalation compounds, Adv. Funct. Mater. 16 (4) (2006) 492–498.

[122] A. Mukhopadhyay, B.W. Sheldon, Deformation and stress in electrode materials for Li-ion batteries, Prog. Mater. Sci. 63 (2014) 58–116.

[123] K. Mizushima, P. Jones, P. Wiseman, J.B. Goodenough, Li_xCoO_2 ($0< x<-1$): A new cathode material for batteries of high energy density, Mat. Res. Bull. 15 (6) (1980) 783–789.

[124] M.S. Whittingham, Lithium batteries and cathode materials, Chem. rev. 104 (10) (2004) 4271–4302.

[125] B.L. Ellis, K.T. Lee, L.F. Nazar, Positive electrode materials for Li-ion and Li-batteries, Chem. Mater. 22 (3) (2010) 691–714.

[126] J.N. Reimers, J. Dahn, Electrochemical and in situ X-ray diffraction studies of lithium intercalation in Li_xCoO_2, J. Electrochem. Soc. 139 (8) (1992) 2091.

[127] J.U. Choi, N. Voronina, Y.K. Sun, S.T. Myung, Recent progress and perspective of advanced high-energy Co-less Ni-rich cathodes for Li-ion batteries: yesterday, today, and tomorrow, Adv. Energy Mater. 10 (42) (2020) 2002027.

[128] W. Li, E.M. Erickson, A. Manthiram, High-nickel layered oxide cathodes for lithium-based automotive batteries, Nat. Energy 5 (1) (2020) 26–34.

[129] H.-J. Noh, S. Youn, C.S. Yoon, Y.-K. Sun, Comparison of the structural and electrochemical properties of layered $Li[Ni_xCo_yMn_z]O_2$ (x = 1/3, 0.5, 0.6, 0.7, 0.8 and 0.85) cathode material for lithium-ion batteries, J. Power Sources 233 (2013) 121-130.

[130] T. Ohzuku, Y. Makimura, Layered lithium insertion material of $LiCo_{1/3}Ni_{1/3}Mn_{1/3}O_2$ for lithium-ion batteries, Chem. Lett. 30 (7) (2001) 642–643.

[131] J. Choi, A. Manthiram, Role of chemical and structural stabilities on the electrochemical properties of layered $LiNi_{1/3}Mn_{1/3}Co_{1/3}O_2$ cathodes, J. Electrochem. Soc. 152 (9) (2005) A1714.

[132] L. de Biasi, A.O. Kondrakov, H. Geßwein, T. Brezesinski, P. Hartmann, J. Janek, Between Scylla and Charybdis: balancing among structural stability and energy density of layered NCM cathode materials for advanced lithium-ion batteries, J. Phys. Chem. C 121 (47) (2017) 26163–26171.

[133] H.-H. Ryu, K.-J. Park, C.S. Yoon, Y.-K. Sun, Capacity fading of Ni-rich Li $[Ni_xCo_yMn_{1-x-y}]O_2$ ($0.6 \leq x \leq 0.95$) cathodes for high-energy-density lithium-ion batteries: bulk or surface degradation? Chem. Mater. 30 (3) (2018) 1155–1163.

[134] W. Liu, P. Oh, X. Liu, M.J. Lee, W. Cho, S. Chae, Y. Kim, J. Cho, Nickel-rich layered lithium transition-metal oxide for high-energy lithium-ion batteries, Ang. Chem. Int. Ed. 54 (15) (2015) 4440–4457.

[135] W. Li, J. Reimers, J. Dahn, In situ x-ray diffraction and electrochemical studies of $Li_{1-x}NiO_2$, Solid State Ionics 67 (1–2) (1993) 123–130.

[136] T. Ohzuku, A. Ueda, M. Nagayama, Electrochemistry and structural chemistry of $LiNiO_2$ (R3m) for 4 volt secondary lithium cells, J. Electrochem. Soc. 140 (7) (1993) 1862.

[137] J.H. Kim, H.H. Ryu, S.J. Kim, C.S. Yoon, Y.K. Sun, Degradation Mechanism of Highly Ni-Rich $Li[Ni_xCo_yMn_{1-x-y}]O_2$ Cathodes with $x > 0.9$, ACS, Appl. Mater. Interfaces 11 (34) (2019) 30936–30942.

[138] P. Trucano, R. Chen, Structure of graphite by neutron diffraction, Nature 258 (5531) (1975) 136–137.

[139] S. Taminato, M. Yonemura, S. Shiotani, T. Kamiyama, S. Torii, M. Nagao, Y. Ishikawa, K. Mori, T. Fukunaga, Y. Onodera, T. Naka, M. Morishima, Y. Ukyo, D.S. Adipranoto, H. Arai, Y. Uchimoto, Z. Ogumi, K. Suzuki, M. Hirayama, R. Kanno, Real-time observations of lithium battery reactions-operando neutron diffraction analysis during practical operation, Sci. Rep. 6 (1) (2016) 28843.

[140] S. Schweidler, L. de Biasi, A. Schiele, P. Hartmann, T. Brezesinski, J. Janek, Volume changes of graphite anodes revisited: a combined operando X-ray diffraction and in situ pressure analysis study, J. Phys. Chem. c 122 (16) (2018) 8829–8835.

[141] J.R. Dahn, Phase diagram of Li_xC_6, Phys. Rev. B Condens. Matter. 44 (17) (1991) 9170–9177.

[142] W.-J. Zhang, Structure and performance of $LiFePO_4$ cathode materials: a review, J. Power Sources 196 (6) (2011) 2962–2970.

[143] B. Zhao, R. Ran, M. Liu, Z. Shao, A comprehensive review of $Li_4Ti_5O_{12}$-based electrodes for lithium-ion batteries: the latest advancements and future perspectives, Mater. Sci. Eng. R Rep. 98 (2015) 1–71.

[144] G. Chen, X. Song, T.J. Richardson, Electron microscopy study of the $LiFePO_4$ to $FePO_4$ phase transition, Electrochem. Solid-State Lett. 9 (6) (2006) A295.

[145] S.Y. Han, C. Lee, J.A. Lewis, D. Yeh, Y. Liu, H.-W. Lee, M.T. McDowell, Stress evolution during cycling of alloy-anode solid-state batteries, Joule 5 (9) (2021) 2450–2465.

[146] M.T. McDowell, S.W. Lee, W.D. Nix, Y. Cui, 25th anniversary article: Understanding the lithiation of silicon and other alloying anodes for lithium-ion batteries, Adv. Mater. 25 (36) (2013) 4966–4985.

[147] M.N. Obrovac, V.L. Chevrier, Alloy negative electrodes for Li-ion batteries, Chem. Rev. 114 (23) (2014) 11444–11502.

[148] T.D. Hatchard, J.R. Dahn, In situ XRD and electrochemical study of the reaction of lithium with amorphous silicon, J. Electrochem. Soc. 151 (6) (2004) A838.

[149] M.N. Obrovac, L. Christensen, Structural changes in silicon anodes during lithium insertion/extraction, Electrochem. Solid-State Lett. 7 (5) (2004) A93.

[150] J. Li, J.R. Dahn, An in situ X-Ray diffraction study of the reaction of Li with crystalline Si, J. Electrochem. Soc. 154 (3) (2007) A156.

[151] D.H. Kim, H.A. Lee, Y.B. Song, J.W. Park, S.-M. Lee, Y.S. Jung, Sheet-type Li_6PS_5Cl-infiltrated Si anodes fabricated by solution process for all-solid-state lithium-ion batteries, J. Power Sources 426 (2019) 143–150.

[152] S. Cangaz, F. Hippauf, F.S. Reuter, S. Doerfler, T. Abendroth, H. Althues, S. Kaskel, Enabling high-energy solid-state batteries with stable anode interphase by the use of columnar silicon anodes, Adv. Energy Mater. 10 (34) (2020) 2001320.

[153] D.H. Tan, Y.-T. Chen, H. Yang, W. Bao, B. Sreenarayanan, J.-M. Doux, W. Li, B. Lu, S.-Y. Ham, B. Sayahpour, Carbon free high loading silicon anodes enabled by sulfide solid electrolytes for robust all solid-state batteries, Science 373 (6562) (2021) 1494–1499.

[154] Y.S. Jung, K.T. Lee, J.H. Ryu, D. Im, S.M. Oh, Sn-carbon core-shell powder for anode in lithium secondary batteries, J. Electrochem. Soc. 152 (7) (2005) A1452.

[155] J. Liu, Z. Bao, Y. Cui, E.J. Dufek, J.B. Goodenough, P. Khalifah, Q. Li, B.Y. Liaw, P. Liu, A. Manthiram, Y.S. Meng, V.R. Subramanian, M.F. Toney, V. V. Viswanathan, M.S. Whittingham, J. Xiao, W. Xu, J. Yang, X.-Q. Yang, J.-G. Zhang, Pathways for practical high-energy long-cycling lithium metal batteries, Nat. Energy 4 (3) (2019) 180–186.

[156] Y. Li, Y. Li, A. Pei, K. Yan, Y. Sun, C.-L. Wu, L.-M. Joubert, R. Chin, A.L. Koh, Y. Yu, Atomic structure of sensitive battery materials and interfaces revealed by cryo–electron microscopy, Science 358 (6362) (2017) 506–510.

[157] X. Zhang, Y. Yang, Z. Zhou, Towards practical lithium-metal anodes, Chem. Soc. Rev. 49 (10) (2020) 3040–3071.

[158] A. Banerjee, X. Wang, C. Fang, E.A. Wu, Y.S. Meng, Interfaces and interphases in all-solid-state batteries with inorganic solid electrolytes, Chem. Rev. 120 (14) (2020) 6878–6933.

[159] T. Krauskopf, F.H. Richter, W.G. Zeier, J. Janek, Physicochemical concepts of the lithium metal anode in solid-state batteries, Chem. Rev. 120 (15) (2020) 7745–7794.

[160] M. Yang, Y. Liu, A.M. Nolan, Y. Mo, Interfacial atomistic mechanisms of lithium metal stripping and plating in solid-state batteries, Adv. Mater. 33 (11) (2021) 2008081.

[161] J. Kasemchainan, S. Zekoll, D. Spencer Jolly, Z. Ning, G.O. Hartley, J. Marrow, P. G. Bruce, Critical stripping current leads to dendrite formation on plating in lithium anode solid electrolyte cells, Nat. Mater. 18 (10) (2019) 1105–1111.

[162] A. Sakuda, A. Hayashi, M. Tatsumisago, Interfacial observation between $LiCoO_2$ electrode and $Li_2S-P_2S_5$ solid electrolytes of all-solid-state lithium secondary batteries using transmission electron microscopy, Chem. Mater. 22 (3) (2010) 949–956.

[163] F. Wu, W. Fitzhugh, L. Ye, J. Ning, X. Li, Advanced sulfide solid electrolyte by core-shell structural design, Nat. Commun. 9 (1) (2018) 1–11.

[164] W. Fitzhugh, L. Ye, X. Li, The effects of mechanical constriction on the operation of sulfide based solid-state batteries, J. Mater. Chem. A 7 (41) (2019) 23604–23627.

[165] Y. Su, L. Ye, W. Fitzhugh, Y. Wang, E. Gil-González, I. Kim, X. Li, A more stable lithium anode by mechanical constriction for solid state batteries, Energy Environ. Sci. 13 (3) (2020) 908–916.

[166] W. Zhang, T. Leichtweiß, S.P. Culver, R. Koerver, D. Das, D.A. Weber, W.G. Zeier, J. Janek, The detrimental effects of carbon additives in $Li_{10}GeP_2S_{12}$-based solid-state batteries, ACS Appl. Mater. Interfaces 9 (41) (2017) 35888–35896.

[167] K. Yoon, J.-J. Kim, W.M. Seong, M.H. Lee, K. Kang, Author correction: investigation on the interface between $Li_{10}GeP_2S_{12}$ electrolyte and carbon conductive agents in all-solid-state lithium battery, Sci. Rep. 8 (1) (2018) 10366.

[168] U.-H. Kim, G.-T. Park, B.-K. Son, G.W. Nam, J. Liu, L.-Y. Kuo, P. Kaghazchi, C. S. Yoon, Y.-K. Sun, Heuristic solution for achieving long-term cycle stability for Ni-rich layered cathodes at full depth of discharge, Nat. Energy 5 (11) (2020) 860–869.

[169] U.-H. Kim, H.-H. Ryu, J.-H. Kim, R. Mücke, P. Kaghazchi, C.S. Yoon, Y.-K. Sun, Microstructure-controlled Ni-rich cathode material by microscale compositional partition for next-generation electric vehicles, Adv. Energy Mater. 9 (15) (2019) 1803902.

[170] C. Wang, R. Yu, S. Hwang, J. Liang, X. Li, C. Zhao, Y. Sun, J. Wang, N. Holmes, R. Li, H. Huang, S. Zhao, L. Zhang, S. Lu, D. Su, X. Sun, Single crystal cathodes enabling high-performance all-solid-state lithium-ion batteries, Energy Storage Mater. 30 (2020) 98–103.

[171] S. Schweidler, M. Bianchini, P. Hartmann, T. Brezesinski, J. Janek, The sound of batteries: an operando acoustic emission study of the $LiNiO_2$ cathode in Li–ion cells, Batter. Supercaps 3 (10) (2020) 1021–1027.

[172] L. de Biasi, A. Schiele, M. Roca-Ayats, G. Garcia, T. Brezesinski, P. Hartmann, J. Janek, Phase transformation behavior and stability of $LiNiO_2$ cathode material for Li-ion batteries obtained from in situ gas analysis and operando X-Ray diffraction, ChemSusChem 12 (10) (2019) 2240–2250.

[173] M. Doyle, J. Newman, Analysis of capacity–rate data for lithium batteries using simplified models of the discharge process, J. Appl. Electrochem. 27 (7) (1997) 846–856.

[174] Y.-K. Sun, Z. Chen, H.-J. Noh, D.-J. Lee, H.-G. Jung, Y. Ren, S. Wang, C.S. Yoon, S.-T. Myung, K. Amine, Nanostructured high-energy cathode materials for advanced lithium batteries, Nat. Mater. 11 (11) (2012) 942–947.

[175] C. Xu, W. Xiang, Z. Wu, Y. Xu, Y. Li, Y. Wang, Y. Xiao, X. Guo, B. Zhong, Highly stabilized Ni-rich cathode material with Mo induced epitaxially grown nanostructured hybrid surface for high-performance lithium-ion batteries, ACS Appl. Mater. Interfaces 11 (18) (2019) 16629–16638.

[176] J. Liu, H. Chen, J. Xie, Z. Sun, N. Wu, B. Wu, Electrochemical performance studies of Li-rich cathode materials with different primary particle sizes, J. Power Sources 251 (2014) 208–214.

[177] H.-H. Ryu, K.-J. Park, D.R. Yoon, A. Aishova, C.S. Yoon, Y.-K. Sun, Li $[Ni_{0.9}Co_{0.09}W_{0.01}]O_2$: a new type of layered oxide cathode with high cycling stability, Adv. Energy Mater. 9 (44) (2019) 1902698.

[178] K.-J. Park, H.-G. Jung, L.-Y. Kuo, P. Kaghazchi, C.S. Yoon, Y.-K. Sun, Improved cycling stability of $Li[Ni_{0.90}Co_{0.05}Mn_{0.05}]O_2$ through microstructure modification by boron doping for Li-ion batteries, Adv. Energy Mater. 8 (25) (2018) 1801202.

[179] J.E. Harlow, X. Ma, J. Li, E. Logan, Y. Liu, N. Zhang, L. Ma, S.L. Glazier, M.M.E. Cormier, M. Genovese, S. Buteau, A. Cameron, J.E. Stark, J.R. Dahn, A Wide Range of Testing Results on an Excellent Lithium-Ion Cell Chemistry to be used as Benchmarks for New Battery Technologies, J. Electrochem. Soc. 166(13) (2019) A3031-A3044.

[180] H.-H. Sun, J.A. Weeks, A. Heller, C.B. Mullins, Nanorod gradient cathode: preventing electrolyte penetration into cathode particles, ACS Appl. Energy Mater. 2 (8) (2019) 6002–6011.

[181] X. Liu, B. Zheng, J. Zhao, W. Zhao, Z. Liang, Y. Su, C. Xie, K. Zhou, Y. Xiang, J. Zhu, Electrochemo-mechanical effects on structural integrity of Ni-rich cathodes with different microstructures in all solid-state batteries, Adv. Energy Mat. 11 (8) (2021) 2003583.

[182] A. Masias, N. Felten, R. Garcia-Mendez, J. Wolfenstine, J. Sakamoto, Elastic, plastic, and creep mechanical properties of lithium metal, J. Mater. Sci. 54 (3) (2019) 2585–2600.

[183] X. Wu, J. Billaud, I. Jerjen, F. Marone, Y. Ishihara, M. Adachi, Y. Adachi, C. Villevieille, Y. Kato, Operando visualization of morphological dynamics in all-solid-state batteries, Adv. Energy Mater. 9 (34) (2019) 1901547.

[184] J. Tippens, J.C. Miers, A. Afshar, J.A. Lewis, F.J.Q. Cortes, H. Qiao, T.S. Marchese, C.V. Di Leo, C. Saldana, M.T. McDowell, Visualizing chemomechanical degradation of a solid-state battery electrolyte, ACS Energy Lett. 4 (6) (2019) 1475–1483.
[185] M. Wang, J.B. Wolfenstine, J. Sakamoto, Temperature dependent flux balance of the Li/$Li_7La_3Zr_2O_{12}$ interface, Electrochim. Acta 296 (2019) 842–847.
[186] Z. Ning, D.S. Jolly, G. Li, R.D. Meyere, S.D. Pu, Y. Chen, J. Kasemchainan, J. Ihli, C. Gong, B. Liu, D.L.R. Melvin, A. Bonnin, O. Magdysyuk, P. Adamson, G. O. Hartley, C.W. Monroe, T.J. Marrow, P.G. Bruce, Visualizing plating-induced cracking in lithium-anode solid-electrolyte cells, Nat. Mater. 20 (2021) 1121–1129.
[187] J.-M. Doux, H. Nguyen, D.H.S. Tan, A. Banerjee, X. Wang, E.A. Wu, C. Jo, H. Yang, Y.S. Meng, Stack pressure considerations for room-temperature all-solid-state lithium metal batteries, Adv. Energy Mater. 10 (1) (2020) 1903253.
[188] C. Lee, S.Y. Han, J.A. Lewis, P.P. Shetty, D. Yeh, Y. Liu, E. Klein, H.-W. Lee, M. T. McDowell, Stack pressure measurements to probe the evolution of the lithium–solid-state electrolyte interface, ACS Energy Lett. 6 (9) (2021) 3261–3269.
[189] J.M. Whiteley, J.W. Kim, C.S. Kang, J.S. Cho, K.H. Oh, S.-H. Lee, Tin networked electrode providing enhanced volumetric capacity and pressureless operation for all-solid-state Li-ion batteries, J. Electrochem. Soc. 162 (4) (2015) A711–A715.
[190] V. Wurster, C. Engel, H. Graebe, T. Ferber, W. Jaegermann, R. Hausbrand, Characterization of the interfaces in $LiFePO_4$/PEO-LiTFSI composite cathodes and to the adjacent layers, J. Electrochem. Soc. 166 (3) (2019) A5410–A5420.
[191] Y. Tang, L. Zhang, J. Chen, H. Sun, T. Yang, Q. Liu, Q. Huang, T. Zhu, J. Huang, Electro-chemo-mechanics of lithium in solid state lithium metal batteries, Energy Environ. Sci. 14 (2) (2021) 602–642.
[192] X. Zhang, Q.J. Wang, K.L. Harrison, K. Jungjohann, B.L. Boyce, S.A. Roberts, P. M. Attia, S.J. Harris, Rethinking how external pressure can suppress dendrites in lithium metal batteries, J. Electrochem. Soc. 166 (15) (2019) A3639–A3652.
[193] A. Gupta, E. Kazyak, N. Craig, J. Christensen, N.P. Dasgupta, J. Sakamoto, Evaluating the effects of temperature and pressure on Li/PEO-LiTFSI interfacial stability and kinetics, J. Electrochem. Soc. 165 (11) (2018) A2801–A2806.
[194] Z. Siroma, T. Sato, T. Takeuchi, R. Nagai, A. Ota, T. Ioroi, AC impedance analysis of ionic and electronic conductivities in electrode mixture layers for an all-solid-state lithium-ion battery, J. Power Sources 316 (2016) 215–223.
[195] N. Kaiser, S. Spannenberger, M. Schmitt, M. Cronau, Y. Kato, B. Roling, Ion transport limitations in all-solid-state lithium battery electrodes containing a sulfide-based electrolyte, J. Power Sources 396 (2018) 175–181.
[196] P. Minnmann, L. Quillman, S. Burkhardt, F.H. Richter, J. Janek, Editors' choice—quantifying the impact of charge transport bottlenecks in composite cathodes of all-solid-state batteries, J. Electrochem. Soc. 168 (4) (2021), 040537.
[197] W.-S. Yoon, K.Y. Chung, J. McBreen, X.-Q. Yang, A comparative study on structural changes of $LiCo_{1/3}Ni_{1/3}Mn_{1/3}O_2$ and $LiNi_{0.8}Co_{0.15}Al_{0.05}O_2$ during first charge using in situ XRD, Electrochem. Commun. 8 (8) (2006) 1257–1262.